

# Modeling phytoplankton blooms and inorganic carbon responses to sea-ice variability in the West Antarctic Peninsula (WAP)

Cristina Schultz<sup>1</sup>, Scott C. Doney<sup>1</sup>, Judith Hauck<sup>2</sup>, Maria Kavanaugh<sup>3</sup>, and Oscar Schofield<sup>4</sup>

<sup>1</sup>University of Virginia

<sup>2</sup>Alfred Wegener Institute Helmholtz Centre for Polar and Marine Research

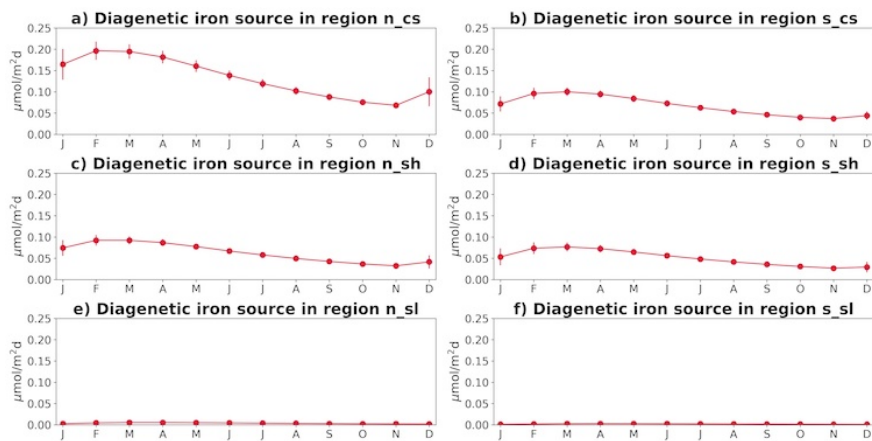
<sup>3</sup>Oregon State University

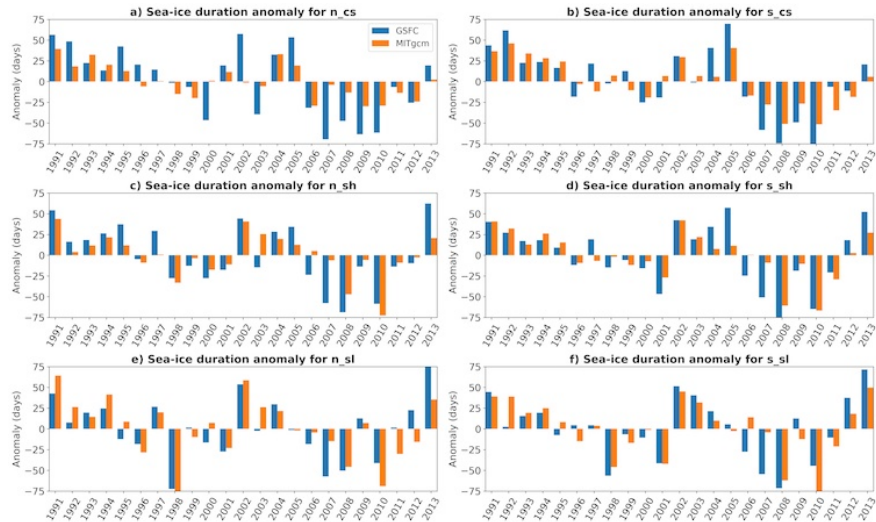
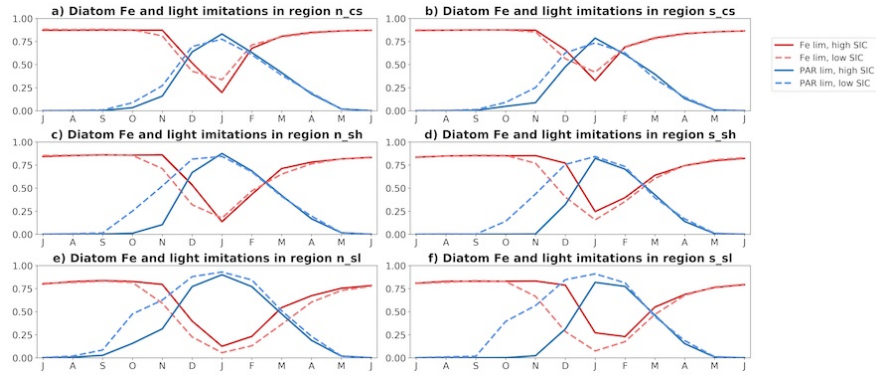
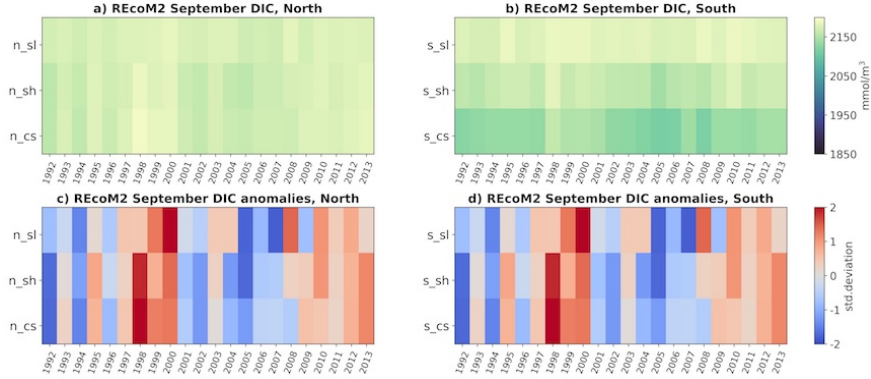
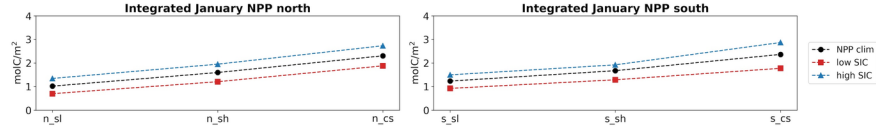
<sup>4</sup>Rutgers University

November 24, 2022

## Abstract

The ocean coastal-shelf-slope ecosystem west of the Antarctic Peninsula (WAP) is a biologically productive region that could potentially act as a large sink of atmospheric carbon dioxide. The duration of the sea-ice season in the WAP shows large interannual variability. However, quantifying the mechanisms by which sea ice impacts biological productivity and surface dissolved inorganic carbon (DIC) remains a challenge due to the lack of data early in the phytoplankton growth season. In this study, we implemented a circulation, sea-ice and biogeochemistry model (MITgcm-REcoM2) to study the effect of sea ice on phytoplankton blooms and surface DIC. Results were compared with satellite sea-ice and ocean color, and research ship surveys from the Palmer Long Term Ecological Research (LTER) program. The simulations suggest that the annual sea-ice cycle has an important role in the seasonal DIC drawdown. In years of early sea-ice retreat there is a longer growth season leading to larger seasonally integrated net primary production (NPP). Part of the biological uptake of DIC by phytoplankton, however, is counteracted by increased oceanic uptake of atmospheric CO<sub>2</sub>. Despite lower seasonal NPP, years of late sea-ice retreat show larger DIC drawdown, attributed to lower air-sea CO<sub>2</sub> fluxes and increased dilution by sea-ice melt. The role of dissolved iron and iron limitation on WAP phytoplankton also remains a challenge due to the lack of data. The model results suggest sediments and glacial meltwater are the main sources in the coastal and shelf regions, with sediments being more influential in the northern coast.





1  
2 **Modeling phytoplankton blooms and inorganic carbon responses to**  
3 **sea-ice variability in the West Antarctic Peninsula (WAP)**  
4

5 **C. Schultz**<sup>1,2,3</sup>, **S. C. Doney**<sup>1</sup>, **J. Hauck**<sup>4</sup>, **M. T. Kavanaugh**<sup>5</sup>, **O. Schofield**<sup>6</sup>  
6

7 <sup>1</sup> University of Virginia, Department of Environmental Sciences, Charlottesville, VA, USA

8 <sup>2</sup> Woods Hole Oceanographic Institution, Woods Hole, MA, USA

9 <sup>3</sup> Massachusetts Institute of Technology, Department of Earth and Atmospheric Sciences,  
10 Cambridge, MA, USA

11 <sup>4</sup> Alfred-Wegener-Institut, Helmholtz-Zentrum für Polar und Meeresforschung, Bremerhaven,  
12 Germany

13 <sup>5</sup> Oregon State University, College of Earth, Ocean, and Atmospheric Sciences, Corvallis, OR, USA

14 <sup>6</sup> Rutgers University, Center for Ocean Observing Leadership, New Brunswick, NJ, USA  
15

16 Corresponding author: Cristina Schultz ([cs3xm@virginia.edu](mailto:cs3xm@virginia.edu))  
17  
18

- 19 • Longer growth season in years of early sea-ice retreat lead to higher seasonally  
20 integrated NPP, despite lower chlorophyll in January
- 21 • Sea ice is important for DIC drawdown by controlling duration of phytoplankton bloom,  
22 air-sea CO<sub>2</sub> fluxes and dilution by meltwater
- 23 • In the WAP, sedimentary iron has a larger role in the northern coast and shelf, glacial  
24 meltwater likely the main source in the south  
25  
26  
27  
28  
29

30

31 **Abstract**

32 The ocean coastal-shelf-slope ecosystem west of the Antarctic Peninsula (WAP) is a biologically  
33 productive region that could potentially act as a large sink of atmospheric carbon dioxide. The  
34 duration of the sea-ice season in the WAP shows large interannual variability. However,  
35 quantifying the mechanisms by which sea ice impacts biological productivity and surface  
36 dissolved inorganic carbon (DIC) remains a challenge due to the lack of data early in the  
37 phytoplankton growth season. In this study, we implemented a circulation, sea-ice and  
38 biogeochemistry model (MITgcm-REcoM2) to study the effect of sea ice on phytoplankton  
39 blooms and surface DIC. Results were compared with satellite sea-ice and ocean color, and  
40 research ship surveys from the Palmer Long Term Ecological Research (LTER) program. The  
41 simulations suggest that the annual sea-ice cycle has an important role in the seasonal DIC  
42 drawdown. In years of early sea-ice retreat there is a longer growth season leading to larger  
43 seasonally integrated net primary production (NPP). Part of the biological uptake of DIC by  
44 phytoplankton, however, is counteracted by increased oceanic uptake of atmospheric CO<sub>2</sub>.  
45 Despite lower seasonal NPP, years of late sea-ice retreat show larger DIC drawdown, attributed  
46 to lower air-sea CO<sub>2</sub> fluxes and increased dilution by sea-ice melt. The role of dissolved iron and  
47 iron limitation on WAP phytoplankton also remains a challenge due to the lack of data. The  
48 model results suggest sediments and glacial meltwater are the main sources in the coastal and  
49 shelf regions, with sediments being more influential in the northern coast.

50

51

52 **1. Introduction**

53

54 The Southern Ocean (south of 44°S) plays a crucial role in the global carbon cycle, acting  
55 as a major sink for modern anthropogenic CO<sub>2</sub> and modulating, on longer time-scales, ocean-  
56 atmosphere CO<sub>2</sub> partitioning through variations in the biological carbon pump, surface nutrient  
57 utilization, and deep-ocean ventilation (Gruber and Doney, 2019). Contemporary air-sea CO<sub>2</sub>  
58 fluxes in the region reflect a combination of natural degassing to the atmosphere and

59 anthropogenic CO<sub>2</sub> uptake (Lenton et al., 2013), with the southernmost latitudes representing  
60 only a small sink. However, large-scale estimates of air-sea CO<sub>2</sub> fluxes do not adequately resolve  
61 the coastal regions of Antarctica, which can be highly productive biologically and act as strong  
62 sinks of anthropogenic carbon (Arrigo et al., 2008). Therefore, a better assessment of the role  
63 of the Southern Ocean in the global carbon cycle relies on improving the understanding of the  
64 air-sea fluxes and biological carbon cycling in the coastal areas of Antarctica and the fate of the  
65 excess carbon.

66         One of these productive coastal regions is the shelf-slope on the West Antarctic  
67 Peninsula (WAP), a sea-ice influenced marine ecosystem with relatively high primary  
68 production and net community production (NCP) during the summer season (Vernet et al.,  
69 2008; Ducklow et al., 2013; Ducklow et al., 2018), and air-sea CO<sub>2</sub> fluxes indicate a strong sink  
70 of atmospheric carbon (Legge et al., 2015; Jones et al., 2017). Although the dissolved inorganic  
71 carbon in the surface ocean is highly variable and controlled by a variety of physical and  
72 biological factors, such as respiration, freshwater inputs, brine rejection and mixing with  
73 subsurface waters rich in dissolved inorganic carbon (DIC; Carrillo et al., 2004; Eveleth et al.,  
74 2017), primary production is estimated to have a large role in controlling DIC during the  
75 summer months (Legge et al., 2015).

76         Along the WAP there are long-term trends in several physical variables, with the last  
77 decades exhibiting a substantial shortening of the sea-ice season (Stammerjohn et al., 2008;  
78 2012), an increase in the surface ocean temperature of the order of 1 °C (Meredith et al., 2005),  
79 and melting of glaciers at an accelerating rate (Cook et al., 2005). Despite the long-term trends,  
80 the duration of the sea-ice season, as well as the intensity of the phytoplankton bloom and the  
81 surface carbon concentrations, show high interannual variability due to the influence of the  
82 Southern Annular Mode (SAM) and El Niño Southern Oscillation (ENSO) in the region (Vernet et  
83 al., 2008; Stammerjohn et al., 2008; 2012; Ducklow et al., 2013, Hauri et al., 2015). Positive  
84 phases of SAM and La Niña events lead to warmer conditions and less sea ice along the WAP,  
85 with colder years and a longer sea-ice season observed in negative SAM and El Niño years.  
86 These modes of climate variability also reinforce each other in this region, with years of

87 associated +SAM/La Niña (-SAM/El Niño) showing even warmer (colder) conditions  
88 (Stammerjohn et al., 2008).

89         Understanding the mechanisms behind the variations in primary productivity and DIC in  
90 the WAP is important not only to quantify its present contribution to the global carbon cycle,  
91 but also to predict the changes that will occur under increased glacial meltwater input and  
92 warmer conditions. Field sampling of the region, however, is limited by the presence of sea ice  
93 and harsh weather during much of the year. The Palmer LTER (Long Term Ecological Research)  
94 project (Ducklow et al., 2012; Ducklow et al., 2013) provides a valuable dataset that includes  
95 physical, biological and chemical variables from cruises performed during the months of  
96 January and February each year since 1993, but data is still limited in time to mid-summer  
97 conditions. While satellite chlorophyll data helps to fill in the gaps in assessing the strength of  
98 the phytoplankton blooms, the data is biased towards ice-free and non-cloudy areas, making it  
99 hard to assess the timing of bloom initiation.

100         Although primary production in the WAP is patchy and can vary by an order of  
101 magnitude from year-to-year (Vernet et al., 2008), some characteristics are observed  
102 consistently. Phytoplankton blooms follow the retreat of sea ice, peaking first in the northern  
103 and offshore areas, and there is a consistent onshore-offshore gradient, with coastal and shelf  
104 waters being up to eight times more productive than offshore regions (Li et al., 2015). The  
105 blooms are dominated by diatoms with secondary contributions from cryptophytes (Schofield  
106 et al., 2017; Brown et al., 2019), and the main mechanism controlling its progression is thought  
107 to be light limitation. Macronutrients are abundant (Kim et al., 2016) and micronutrient iron  
108 limitation is not observed in the coastal areas (Carvalho et al., 2016), although it is expected in  
109 the offshore regions (Arrigo et al., 2008; Li et al., 2015, Annett et al., 2017). Summer DIC  
110 measurements show lower concentrations than would be expected from dilution due to  
111 meltwater and glacial input, indicating that they are influenced by biological net community  
112 production (Hauri et al., 2015; Legge et al., 2015).

113         Given the high interannual variability of the blooms and the patchiness observed during  
114 individual years, however, the importance of different processes in controlling the timing and  
115 intensity of the bloom, as well as long-term trends, remain unknown. The long-term trends in

116 chlorophyll based on satellite ocean color observations (decade-decade) were estimated to be  
117 negative in the northern part of the grid and positive in the southern part (Montes-Hugo et al.,  
118 2010), related to sea ice decrease, winds, and changes in mixed layer depth (MLD). With less  
119 sea ice the northern part of the WAP, where more light is available throughout the year, the  
120 region is more exposed to wind mixing, which deepens the MLD and lowers photosynthetically  
121 available radiation (PAR). In the southern WAP, areas that were previously completely covered  
122 by sea ice had an increase in PAR and higher productivity. Kim et al. (2018), however, found a  
123 trend of increase in chlorophyll values for near-shore time-series sites at Palmer Station and  
124 Potter Cove (in the northern part of the WAP), and a decrease in Rothera Station, in the  
125 southern region, driven by a sea-ice rebound that started in 2009.

126 While macronutrients are known to be abundant in the WAP, the concentrations of  
127 dissolved iron (dFe) and their sources are also not well constrained. It is unknown, therefore,  
128 the role dFe plays in controlling the intensity and patchiness of the bloom. This is due to the  
129 fact that collecting *in situ* seawater dFe data is a challenging process, and this micronutrient is  
130 undersampled in the WAP compared to macronutrients and biological data. Studies available,  
131 performed with relatively small datasets, reach conflicting conclusions regarding the source of  
132 dFe and how it limits primary production in different places and seasons.

133 Arrigo et al. (2017), using data from a late spring cruise, observed a correlation between  
134 dFe and reduced sea ice, indicating that ice melt could be a source of iron. One caveat,  
135 however, is that freshwater lenses were not linked to the higher dFe concentrations. Annett et  
136 al. (2017), using dFe and oxygen isotope data from the Palmer LTER project from 2010 to 2012,  
137 found that higher dFe concentrations were correlated with glacial freshwater content,  
138 indicating that in coastal and shelf waters glacial runoff was the major source of iron. In a study  
139 aimed at understanding the role of the Palmer Deep Canyon in providing iron to fuel  
140 phytoplankton bloom, Sherrell et al. (2018) found that high dFe was linked to sediment sources  
141 in coastal areas, which were transported to the shelf. This latter study found no connection  
142 between high dFe and glacial input, arguing that sources might differ in different locations or  
143 that vertical mixing might have muddled the interpretation of the freshwater sources in the  
144 Annett et al. (2017) study.

145 It has been established that lower DIC concentrations are associated with higher  
146 primary production in the late summer (Hauri et al., 2015; Legge et al., 2017), it is not clear how  
147 these two variables co-vary throughout the season. Although normalizing DIC to salinity helps  
148 to estimate the biological effect of drawdown by roughly correcting for dilution, variations in  
149 MLD change the expected end-member concentrations for DIC and salinity throughout the  
150 season through mixing with DIC-rich and more saline sub-surface waters.

151 In this study, we use a coupled ocean circulation, sea-ice and biogeochemistry model to  
152 fill some of the gaps in the understanding of the mechanisms controlling phytoplankton bloom  
153 and its impact on the surface DIC concentration in the WAP. We compare the model results to  
154 cruise data from the Palmer LTER project and to satellite data to validate the model results, and  
155 discuss some of the limitations from each method due to the spatial and temporal coverage.

156

## 157 **2. Methods**

158

### 159 **2.1 Model description**

160

161 The ocean circulation and sea-ice model used for this study is a regional domain version  
162 of the Massachusetts Institute of Technology General Circulation Model (MITgcm), with a  
163 hydrostatic setup that includes embedded sea-ice and ice-shelf modules. The grid used, shown  
164 in Figure 1, covers the region extending from 74.7°S, 95°W in the southwest to 55°S, 55.6°W in  
165 the northeast, with a horizontal resolution of 0.2° of longitude and ranging from 0.0538° to  
166 0.1147° latitude. On the vertical, it uses z-level (fixed depth) with 50 layers spaced every 10 m  
167 for the first 120 m. The atmospheric forcings were obtained from the ERA-Interim reanalysis  
168 (Dee et al., 2011) with a horizontal resolution of 1.5° in latitude and longitude and a 6-hour  
169 interval. Freshwater runoff representing melt of land-based ice and iceberg calving and melting  
170 is provided with monthly climatological estimates, using the values estimated by Van Wessem  
171 et al. (2016) distributed uniformly along the coast and linearly decreasing from land out to 100  
172 km. The grid used is shown in Figure 1, and more details on the implementation of the ocean

173 physical circulation and sea-ice models are described in Regan et al. (2018) and Schultz et al.  
174 (2020).

175 The biogeochemical model used is the Regulated Ecosystem Model version 2 (REcoM2),  
176 described in Hauck et al. (2013,2016). REcoM2 has 21 components, including two  
177 phytoplankton groups (diatoms and small phytoplankton), one zooplankton group and organic  
178 and inorganic forms of the main nutrients (iron, nitrogen, silica and carbon). Although not  
179 added as a group, bacteria functionality is represented via remineralization. Emphasis is given  
180 to phytoplankton physiology, with variable cellular stoichiometry and physiological rates that  
181 depend on the intracellular ratios of nitrogen to carbon (N:C), chlorophyll to carbon (Chl:C) and  
182 silica to carbon (Si:C). Phytoplankton chlorophyll is calculated as a function of irradiance and  
183 nitrogen assimilation, degraded at a constant rate, and lost by aggregation and grazing. A  
184 parameterization to include non-linearities in PAR due to the influence of partial sea-ice  
185 coverage was added following Long et al. (2015).

186 The sources of DIC are respiration, remineralization of detritus and dissolution of  
187 calcium carbonate, while sinks are fixation by primary production and formation of calcium  
188 carbonate. Alkalinity increases by nitrogen assimilation and dissolution of calcium carbonate,  
189 and decreases by remineralization and calcification. Air-sea CO<sub>2</sub> fluxes are calculated with code  
190 based on the Ocean Carbon-Cycle Model Intercomparison Project (OCMIP), which uses a  
191 quadratic relationship with wind based on Wanninkhof (1992). The surface CO<sub>2</sub> concentration is  
192 calculated at every time-step using simulated DIC, alkalinity, temperature and salinity, and the  
193 gas exchange is treated as a boundary condition for DIC.

194 Total dissolved iron (dFe) is assumed to be the sum of inorganic bound and organic  
195 complexed (FeL, where L is a ligand) iron. These two forms are in equilibrium according to:

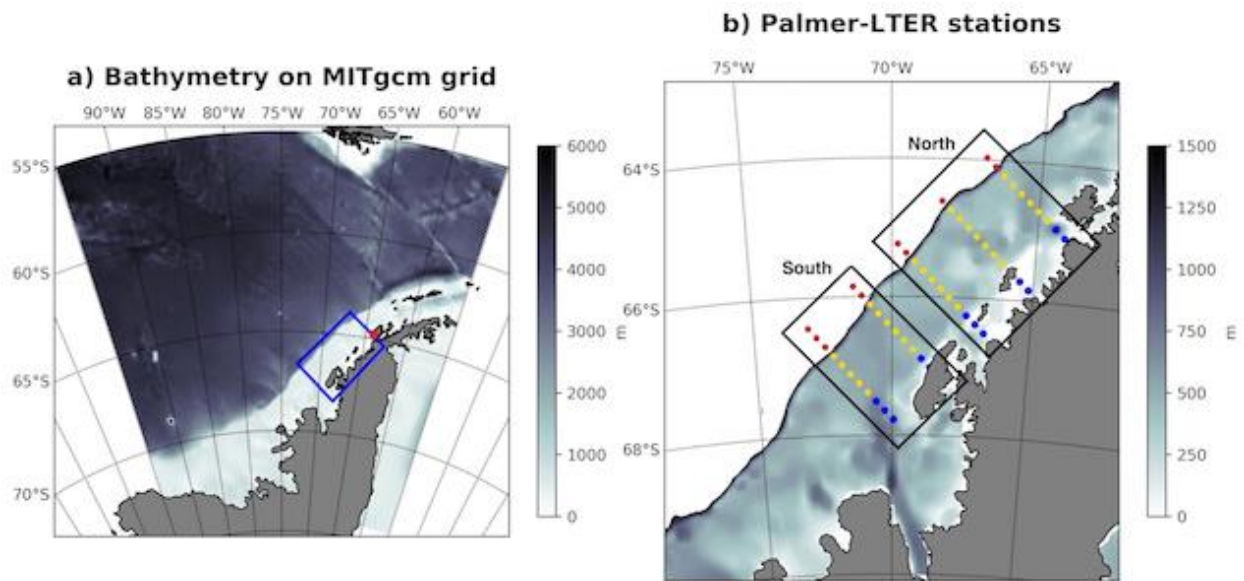
$$K_{FeL} = \frac{Fe' \times L}{FeL} \quad (1)$$

197  
198  
199 where  $K_{FeL}$  is the equilibrium constant and Fe' is the concentration of free iron. Iron is added to  
200 the model via atmospheric deposition and as glacial input, and internal model sources include

201 respiration, remineralization (including diagenetic sediment source) and heterotrophic  
202 excretion, while sinks are represented by scavenging (proportional to detritus concentration)  
203 and photosynthesis.

204

205



206

207 **Figure 1:** a) Map of model bathymetry for the full Southern Ocean sector for the West Antarctic  
208 Peninsula (WAP) with the region of Palmer-LTER cruises marked in the blue rectangle and Palmer Station  
209 marked in the red circle, and b) a larger scale map of coastal-shelf-slope (WAP) overlain with locations of  
210 the Palmer-LTER cruise sampling stations. Blue dots represent the coastal points sampled, yellow dots  
211 represent the shelf points sampled, and red dots represent the slope points sampled. The transect lines  
212 in the southern region are lines 200 (southernmost) and 300, and the transect lines in the northern  
213 region are 400, 500 and 600 (northernmost). Sub-regions analyzed are named northern coastal (n\_cs),  
214 northern shelf (n\_sh), northern slope (n\_sl), southern coastal (s\_cs), southern shelf (s\_sh) and southern  
215 slope (s\_sl).

216

## 217 **2.2 Initial and boundary conditions for REcoM2**

218

219 Initial and boundary conditions for dissolved inorganic nitrogen and silicate (DIN and  
220 DSi) were obtained from the World Ocean Atlas 2013, version 2 (WOA13v2, Garcia et al., 2013).  
221 Monthly climatologies were used from the surface to 500 m, with annual climatology applied

222 below this depth. DIC and alkalinity were obtained from the 1° resolution gridded Global Ocean  
223 Data Analysis Project version 2 (GLODAPv2, Key et al., 2015), with DIC representing  
224 contemporary concentrations centered in 2002 (Lauvseth et al., 2016). Atmospheric CO<sub>2</sub>  
225 remains constant, at 380 ppm. Since dFe data is scarce, the initial and boundary conditions for  
226 this nutrient were obtained from a version of MITgcm-REcoM2 configured globally without the  
227 Arctic region, described in Hauck et al. (2016).

228 Atmospheric deposition and glacial sources of dFe are also represented in the model.  
229 Dust deposition is derived from the Model of Atmospheric Transport and Chemistry (MATCH),  
230 detailed in (Luo et al., 2008). Glacial inputs could be a significant source of iron to the region,  
231 but there is a lack of data on glacial concentrations of this micronutrient. Annett et al. (2017)  
232 estimated meteoric concentrations of dFe of 102 nmol/kg based on the difference of meteoric  
233 water (obtained from oxygen isotopes) and seawater dFe measurements performed between  
234 2011 and 2012. The high concentrations are due to a source mechanism involving dFe-enriching  
235 subglacial processes and glacial meltwater streams. To avoid modifying the code, and taking  
236 advantage of the fact that input of freshwater is done at the surface, the glacial input of dFe  
237 was calculated to scale to the surface runoff at a concentration of 100 nmol/kg, but added to  
238 the same file as the atmospheric deposition. Although the glacial dFe sources include seasonal  
239 variation, a caveat of this approach is that neither glacial inputs of freshwater or dFe include  
240 interannual variability.

241

### 242 **2.3 Experiment description**

243

244 The historical physical-biogeochemical simulation builds upon an existing ocean-sea ice  
245 physical hindcast simulation with the WAP MITgcm (Schultz et al., 2020). The model physics is  
246 forced by atmospheric reanalysis at the surface, seasonally-varying glacial freshwater input  
247 from the Peninsula, and simulated ocean physics and sea-ice climatologies at the lateral  
248 boundaries from a large-scale, low-resolution circumpolar MITgcm simulation (Holland et al.,  
249 2014). Schultz et al. (2020) present a detailed assessment of the physical model behavior and  
250 skill in terms of the geographic patterns, seasonal cycle, and interannual variability ocean mixed

251 layer depth (MLD), sea-ice concentration (SIC) and freshwater dynamics for the WAP coastal-  
252 shelf-slope region. Overall the model performs well in capturing regional sea-ice variations from  
253 satellite observations, reflecting local thermodynamics of sea-ice formation and melt and wind-  
254 driven sea-ice advection and convergence. The model also does a credible job in simulating  
255 summertime MLD patterns found in the Palmer LTER CTD data set, though the simulated MLDs  
256 tend to be biased somewhat shallow compared to the field data. MLD reflects the complex  
257 interactions of wind-driven mixing, seasonal heating and cooling, brine rejection and sea-ice  
258 melt, and lateral circulation, and the MLD biases were improved to some extent with better  
259 model treatments of Langmuir circulation and air-sea ice drag.

260 The physical-biogeochemical model was integrated for 31 years, from 1984 until 2014 in  
261 a similar fashion to the physics-only simulation. The first seven years of integration (1984-1990)  
262 are considered spin-up and the results are analyzed from 1993 (first year of the summer  
263 Palmer-LTER cruises) onward. Diagnostic outputs for simulated physics, nutrients, chlorophyll,  
264 net primary production (NPP), DIC and air-sea CO<sub>2</sub> fluxes were saved every 5 days.

265 Two passive tracer experiments were conducted to assess whether sediment diagenetic  
266 sources of dFe to the water column could impact the concentration in the mixed layer. For  
267 these experiments, the climatological monthly mean fluxes of dFe from sediment to the water  
268 column were calculated, and it was determined that in the coastal and shelf waters there is a  
269 seasonal difference, with more iron being released late summer and less in the spring (Figure  
270 S1). This cycle reflects the phytoplankton bloom with an added lag, given it takes time for  
271 organic matter to reach the bottom and be remineralized. The first passive tracer experiment  
272 used a tracer that accounted for the total climatological amount of iron being released from the  
273 sea floor during the month of February. At every grid point, a diagenetic dFe concentration  
274 anomaly ( $\mu\text{mol}/\text{m}^3$ ) was computed for the bottom layer grid cell assuming that all of sediment  
275 Fe flux ( $\mu\text{mol}/\text{m}^3/\text{d}$ ) for the entire month of February accumulated in the bottom layer. The  
276 tracer was released at the bottom layer in the first day of February 1991, after the spin-up, and  
277 the concentration of the passive tracer was tracked during the next year. A second experiment  
278 used the same approach but using the diagenetic concentration of dFe of July, and released the  
279 tracer in the first day of July, 1991.

280

## 281 **2.4 Calculation of DIC-derived Net Community Production (NCP)**

282

283 The metabolic balance of the whole ecosystem is determined by NCP, which also  
284 governs the potential for biomass accumulation in the and carbon storage in the system. NCP is  
285 used, in this study, to assess the influence of primary production in the DIC drawdown  
286 throughout the warm season in the WAP. Since NCP is not a diagnostic variable of the model, it  
287 was calculated from the DIC drawdown between September and January. September was  
288 chosen as the start of the season since it is the earliest the phytoplankton bloom can start. For  
289 each station, the total DIC inventory for each month was calculated as the vertically integrated  
290 DIC from the September MLD to the surface. Since the mixed layer shoals during the period  
291 considered, using the September MLD guarantees that vertical mixing effects will not influence  
292 the inventory calculations performed.

293 The total DIC drawdown was then corrected for air-sea CO<sub>2</sub> fluxes and for dilution by  
294 sea-ice melt. The air-sea CO<sub>2</sub> flux is a diagnostic of the model, and the dilution by sea-ice melt  
295 was calculated using a salinity mixing curve. The hypothetical DIC inventory (integrated from  
296 the September MLD to the surface) at the end of the season (January) in the case where melt  
297 was the only process affecting it would be:

298

$$Int\_DIC_{dil} = \frac{MLD_{Sep} \times \int_{MLD}^0 [DIC]_{Sep}}{(MLD_{Sep} + melt_{Sep-Jan})}$$

299

(2)

300 where  $MLD_{Sep}$  is the September MLD,  $\int_{MLD}^0 [DIC]_{Sep}$  is the vertically integrated DIC in  
301 September (from bottom of MLD to the surface), and  $melt_{Sep-Jan}$  is the total sea-ice melt  
302 during the season (September to January), given in meters. For this calculation, it is assumed  
303 that sea-ice had a DIC concentration of zero. The DIC drawdown due to sea-ice melt, then,  
304 would be:

305

$$\Delta Int\_DIC = \int_{MLD}^0 [DIC]_{sep} - Int\_DIC_{ait} \quad (3)$$

306

307

308 Once corrected for atmospheric fluxes and melt, the remaining DIC drawdown is due to  
 309 biological activity and therefore can be equated to NCP. The seasonally integrated (September  
 310 to January) NCP, therefore is calculated as:

311

$$NCP_{SONDJ} = \Delta DIC_{SONDJ} - \Delta Int\_DIC - F_{CO_2} \quad (4)$$

312

313

314 where  $\Delta DIC_{SONDJ}$  is the total DIC drawdown and  $F_{CO_2}$  is the air-sea  $CO_2$  flux. The DIC-  
 315 calculated NCP is then compared to NPP, which is a diagnostic variable from the model. These  
 316 calculations were done for each station and averaged for each sub-region.

317

318

## 319 **2.5 Data used for skill assessment**

320

321 The Palmer LTER started in 1991 and has collected physical, biological and chemical data  
 322 along the WAP since then (<http://pal.lternet.edu/>). The data include semiweekly water-column  
 323 sampling near Palmer Station on the southern end of Anvers Island from October through  
 324 March and an oceanographic cruise in January-February each year since 1993 (Ducklow et al.,  
 325 2013). The data collected during the cruises include CTD (conductivity, temperature and depth)  
 326 casts, chlorophyll-a concentration, zooplankton abundance, DIC, alkalinity and nutrients. While  
 327 Palmer Station has higher temporal resolution on the data, the station data is more affected by  
 328 islands, near-shore bathymetry and synoptic scale phenomena that are not captured by the  
 329 model. The cruise sampling grid is too coarse to resolve mesoscale features given the short  
 330 Rossby radius on the shelf, a conclusion that is supported by studies using underway data from  
 331 Palmer LTER cruises (Eveleth et al., 2017). Individual sampling stations can also be affected by

332 phenomena such as the passage of icebergs, which will not be captured by the model.  
333 Clustering the cruise stations in sub-regions and calculating the climatological values and their  
334 anomalies makes it more likely that the data will represent the seasonal variations at a larger  
335 spatial scale; and could therefore be more accurately compared to the model data.

336 This study uses data from lines 200 to 600 of the Palmer LTER grid, spanning 500 km  
337 along the coast and 250 km across the shelf. As shown in Figure 1b, the across-shelf transects  
338 are separated by 100 km, with stations 20 km apart in each transect. All the data is available on  
339 the project web page (<http://pal.lter.edu/data/>). Not all stations are sampled for all variables  
340 measured by the project each year, and each measurement does not necessarily reflect the  
341 mean state of the water column during the summer. To decrease the influence of short-term  
342 and small-scale processes, the cruise data was divided in north (lines 400 to 600) and south  
343 (lines 200 and 300) regions, and into coastal, shelf and slope regions, based on bathymetry. Six  
344 different regions are therefore analyzed: northern coastal (n\_cs), northern shelf (n\_sh),  
345 northern slope (n\_sl), southern coastal (s\_cs), southern shelf (s\_sh) and southern slope (s\_sl).

346 Level 2 remote sensing reflectances (Rrs) from Aqua-MODIS (v. 2018) and SeaWiFs  
347 (v.2018) spanning 1997- 2018 were downloaded from NASA Goddard and binned to a common  
348 10 km grid (Kavanaugh et al., 2015). Chlorophyll-a concentration was calculated per image  
349 using an algorithm tuned specifically for the WAP (Dierssen and Smith, 2000). While this  
350 algorithm was tested during SeaWiFs era, the superior skill has been confirmed with vicarious  
351 comparisons using 1 km Aqua-MODIS data and modern in situ chlorophyll-a from recent Palmer  
352 LTER station and cruise data (Kavanaugh et al., 2015). As the WAP can experience multiple  
353 overflights per day, a daily composite was calculated over the grid, from which an 8 -day and  
354 monthly averages was calculated using geometric means. SeaWiFs and MODIS time series were  
355 merged using the method of Kavanaugh (et al., 2018), which applies a per-pixel seasonal  
356 correction to SeaWiFs data.

357 Sea-ice satellite images are obtained from GSFC (Goddard Space Flight Center)  
358 Bootstrap algorithm (Comiso, 2017). Climatological and monthly mean sea-ice concentration  
359 (SIC) are calculated from binned 8-day means with horizontal resolution of 0.2 degrees in  
360 latitude and longitude. Onset time of sea-ice advance is chosen to be the day in which the

361 average SIC of all the stations in each Palmer LTER sub-region reaches at least 0.15 (15% of the  
362 area covered by sea ice) for 5 days in a row. Sea-ice retreat is assumed to be the last day in  
363 which SIC is greater than 0.15 for the ice season. Further details are provided in Stammerjohn  
364 (2008; 2012).

365

### 366 **3 Results**

367

#### 368 **3.5 Iron sources in the model**

369

370 Given the low temporal and spatial coverage of available in situ dFe data, questions  
371 regarding the mechanisms that supply this micronutrient to different regions in the WAP, as  
372 well as how limiting iron is to primary production, still persist. While Arrigo et al. (2017) argues  
373 that sea ice could be a major source during early spring, Annett et al (2017) found that glacial  
374 meltwater was associated with higher dFe and Sherrell et al. (2018) found that dFe in coastal  
375 areas was supplied by sediment sources near Palmer Deep canyon.

376 In the model, atmospheric deposition of iron is negligible, and the sources of dFe to the  
377 mixed layer are glacial input, entrainment from below the mixed layer or transport from other  
378 locations, including from the bottom layer which is enriched via sediment diagenetic processes.  
379 The glacial source of dFe is prescribed; climatological estimates of freshwater runoff were  
380 uniformly distributed along the coast and decreasing linearly in volume from the shore out to  
381 100 km from the coast, and a concentration of 100 nM of dFe was added to this runoff. The  
382 entrainment from below the mixed layer was calculated from the monthly climatology using  
383 the equation:

384

$$F_{ent} = \frac{dMLD}{dt} \Delta[dFe]$$

(5)

385

386 where  $dMLD/dt$  is the deepening of the MLD from month to month and  $\Delta[dFe]$  is the dFe  
387 concentration difference between the mixed layer and the layer below. Equation 2 is only valid  
388 for periods of deepening mixed layer, since the subsurface dFe concentrations are consistently

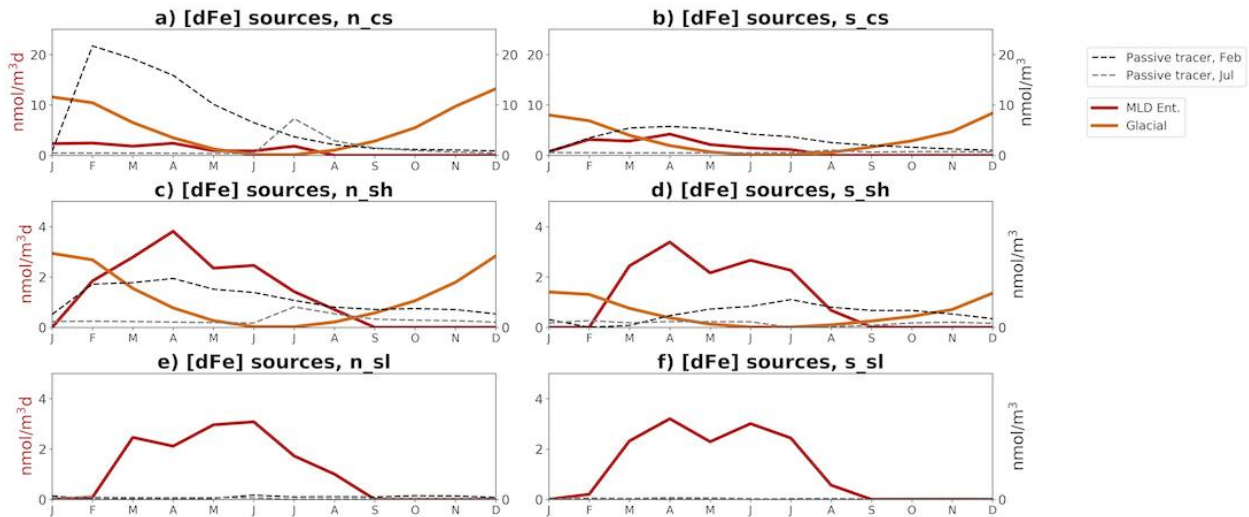
389 higher than the concentrations in the mixed layer. The fluxes during shoaling periods were set  
390 to zero, since no dFe was added to the mixed layer. Estimating the influence of sediment dFe at  
391 a certain location is more difficult given the role of circulation and transformation processes  
392 while iron makes its way from the sediment to the mixed layer. Using the concentration of the  
393 passive tracer experiments described in the Methods (Section 2.3) can give us an idea of where  
394 this source could be significant, but quantifying how much dFe comes from the sediment is not  
395 the goal of this experiment given that, unlike a passive tracer, iron could be consumed and  
396 transformed along the way from the sediment to the sub-regions of interest.

397 Figure 2 shows the flux of glacial and entrainment sources to the mixed layer (in orange,  
398 red), and the concentration of passive tracers in the ML during the year following their release  
399 (in black). Diagenetic dFe is a major source only in the northern coastal region, having a smaller  
400 impact in the southern coast and northern shelf, and no impact in the southern shelf and slope  
401 regions. Glacial sources, as expected from the design of the forcing files, has diminishing  
402 importance from the coast to the slope areas. Entrainment from below the mixed layer is a  
403 source of iron from late summer to early spring in the shelf and slope, but this mechanism of  
404 iron enrichment is halted from September through January while the mixed layer shoals.

405 This analysis shows that there is an (expected) difference in terms of iron supply  
406 between coastal, shelf and slope areas, but also that there is a difference between the northern  
407 and southern regions, stronger in the coastal region. The model results indicate that in the  
408 northern coastal area, which is shallower and more influenced by circulation around the  
409 islands, sedimentary processes are major source of dFe, while in the south glacial input is the  
410 dominant source of dFe. This difference validates the hypothesis suggested in Sherrell et al.  
411 (2018) that the discrepancies found between their study and the study of Annett et al. (2017)  
412 could be due to different sources having different impacts throughout the WAP. While Annett  
413 et al. (2017) found the highest correlations between meteoric water and dFe in the southern  
414 part of the grid, the study of Sherrell et al. (2018) was aimed at understanding Palmer Deep,  
415 located near-shore and closest to line 600 (north).

416

417



418

419 **Figure 2:** MITgcm-REcoM simulated glacial fluxes of dFe (orange), dFe entrainment from below  
420 the ML (red) in nmol/m<sup>3</sup>d (y-axis scale on the left of plot). Dotted lines in black and gray  
421 represent the concentration of passive tracers (January and July, respectively) released at the  
422 bottom in the mixed layer of each sub-region in the year following their release (y-axis scale on  
423 the right of plot). Notice the different y-axis scales for coastal region compared to shelf and  
424 slope regions.

425

426 While we suspect that the subsurface concentration of dFe in the model is higher  
427 offshore than would be observed due to the values used for the initial and boundary conditions,  
428 there is no data to validate this assumption. There are also significant uncertainties about the  
429 transformation and scavenging rates for dFe along the WAP. If the mechanisms represented in  
430 the model are correct, however, the higher iron concentrations found in regions of low sea ice  
431 in the slope regions, as found in Arrigo et al. (2008), would be explained by the fact that low sea  
432 ice concentration promotes mixing of surface waters with iron-rich subsurface waters by  
433 enhancing wind action, not due to iron released from sea ice.

434

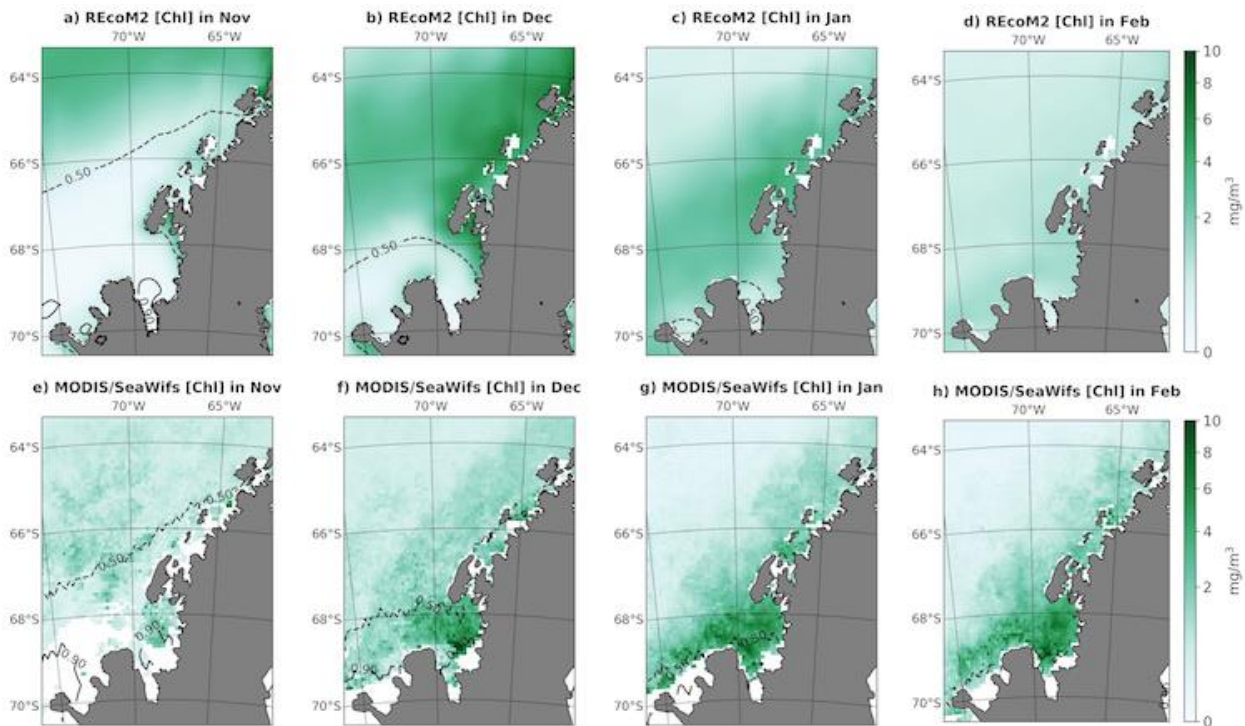
### 435 3.6 Model skill in reproducing phytoplankton bloom climatology

436

437 To assess the model skill in reproducing the observed bloom climatology, we compared  
438 the monthly mean surface chlorophyll concentrations and SIC from the model with the monthly  
439 mean satellite data, shown for the period between November and February in Figure 2. Similar  
440 to observations, the simulated progression of the bloom follows the retreat of sea ice from  
441 offshore to onshore and from north to south. In parts of the grid, particularly the southern shelf  
442 and slope, however, the start of the bloom happens later in the model due to a delay in the  
443 modeled sea-ice retreat in this region, which leads to lower PAR at the beginning of the season.

444 The model also simulates the onshore-offshore gradient in surface chlorophyll seen in  
445 the observations, with higher concentration in the coastal and shelf areas. The simulated  
446 chlorophyll, however, has higher values in the coast and shelf regions in December and in the  
447 offshore areas throughout the season. It is thought that primary production offshore is limited  
448 by iron (Garibotti et al., 2005), which is not the case in the model as can be seen in the seasonal  
449 progression of the limitation terms, shown in Figure S2. Given the lack of iron data in the  
450 region, particularly farther from the coast, the understanding of the iron dynamics is limited  
451 and it is not possible to derive initial and boundary conditions from observations. Therefore, it  
452 is possible that the model derived subsurface dFe, which reaches concentrations of 0.75  
453  $\mu\text{mol}/\text{m}^3$  in all sub-regions, is too high; leading to the higher chlorophyll values. The model also  
454 shows a sharper decrease in chlorophyll from January to February compared to the satellite  
455 data.

456



458

459 **Figure 3:** MITgcm-REcoM2 (top) and MODIS/SeaWifs (bottom) climatological surface chlorophyll  
 460 concentration for November, December, January and February (left to right). Black dashed line shows  
 461 SIC equal 0.5, and black full lines show SIC of 0.9

462

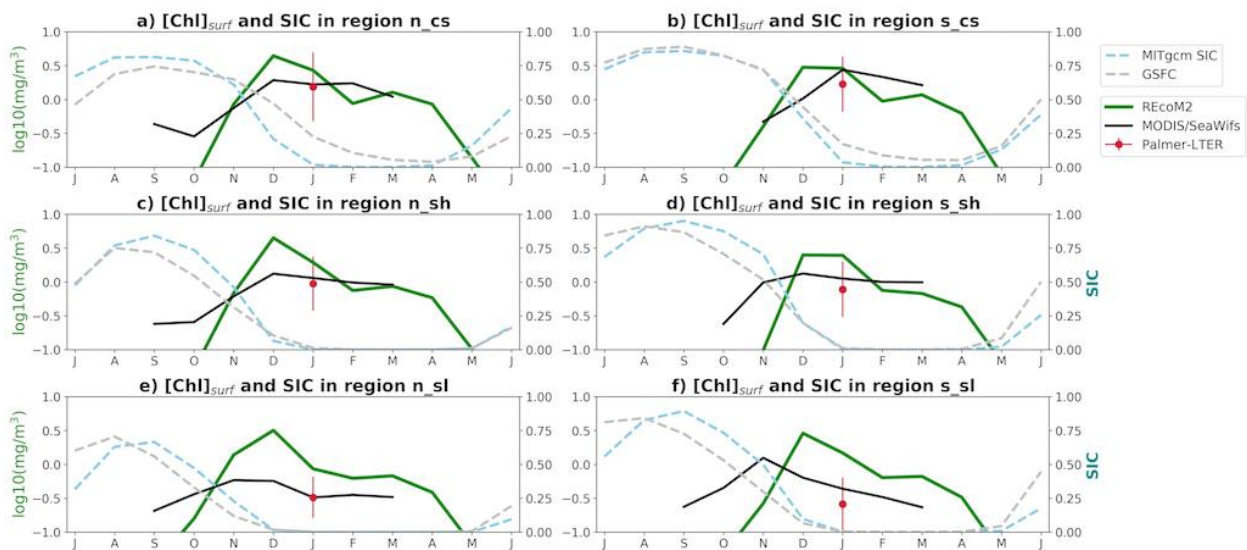
463 For each Palmer LTER survey cruise station, the data from the nearest model and  
 464 satellite grid points were extracted, and the evolution of the surface chlorophyll concentrations  
 465 and SIC are shown in Figure 4 along with the Palmer LTER surface chlorophyll data, assumed to  
 466 be the January mean. Although the Palmer LTER data only has one data point per station each  
 467 year, making it hard to assess whether each data point it is representative of the regional values  
 468 for that year, the climatological mean (calculated as the geometric mean of all the stations for  
 469 each sub-region between 1993-2014) is comparable to the satellite climatology. The Palmer  
 470 LTER and satellite data are similar in the northern region, while in the south the satellite shows  
 471 slightly higher surface chlorophyll concentrations.

472

473 From Figure 4 it is also seen that simulated January chlorophyll concentrations are  
 closer to the observed values in the coastal regions, particularly in the southern coast where

474 sea-ice advance and retreat is better represented. Although the simulated bloom starts later  
 475 than observed in the satellite data, the timing of the peak of the bloom coincides with the  
 476 observations in much of the grid, with the exception of the southern coast and slope. The  
 477 model chlorophyll values also show the lowest summer values in February, with increased  
 478 concentrations in March. Given that PAR availability in March is lower than in February, this can  
 479 be attributed to iron limitation. The iron limitation terms are lowest in January, indicating high  
 480 consumption during this month and leading to lower chlorophyll concentrations in early  
 481 February before iron is replenished by deepening of the mixed layer.

482  
 483



484  
 485 **Figure 4:** MITgcm-REcoM2 (light blue dashed line) and GSFC (gray dashed line) climatological monthly  
 486 sea ice concentration; MITgcm-REcoM2 (green) and MODIS/SeaWifs (black) log-transformed  
 487 climatological monthly surface chlorophyll concentration; Palmer-LTER  $\log_{10}$ -transformed climatological  
 488 surface chlorophyll concentration (red dot, plotted as January mean), during July-June, for regions n\_cs  
 489 (a), s\_cs (b), n\_sh (c), s\_sh (d), n\_sl (e), s\_sl (f). Vertical lines represent standard deviation.

490

### 491 3.7 Interannual variability of the phytoplankton bloom

492

493 To analyze the interannual variability of the phytoplankton bloom, the anomalies  
 494 (relative to the climatology) of surface chlorophyll concentration were calculated for each sub-

495 region and for each dataset (Figure 5). For this comparison, the January monthly means were  
496 used for the satellite and model data, and the reference period from which the anomaly was  
497 calculated was from 1998, when satellite measurements started, until 2014. The figure shows  
498 discrepancies among the datasets, which could be attributed to the limited data collection and  
499 the patchiness of the bloom.

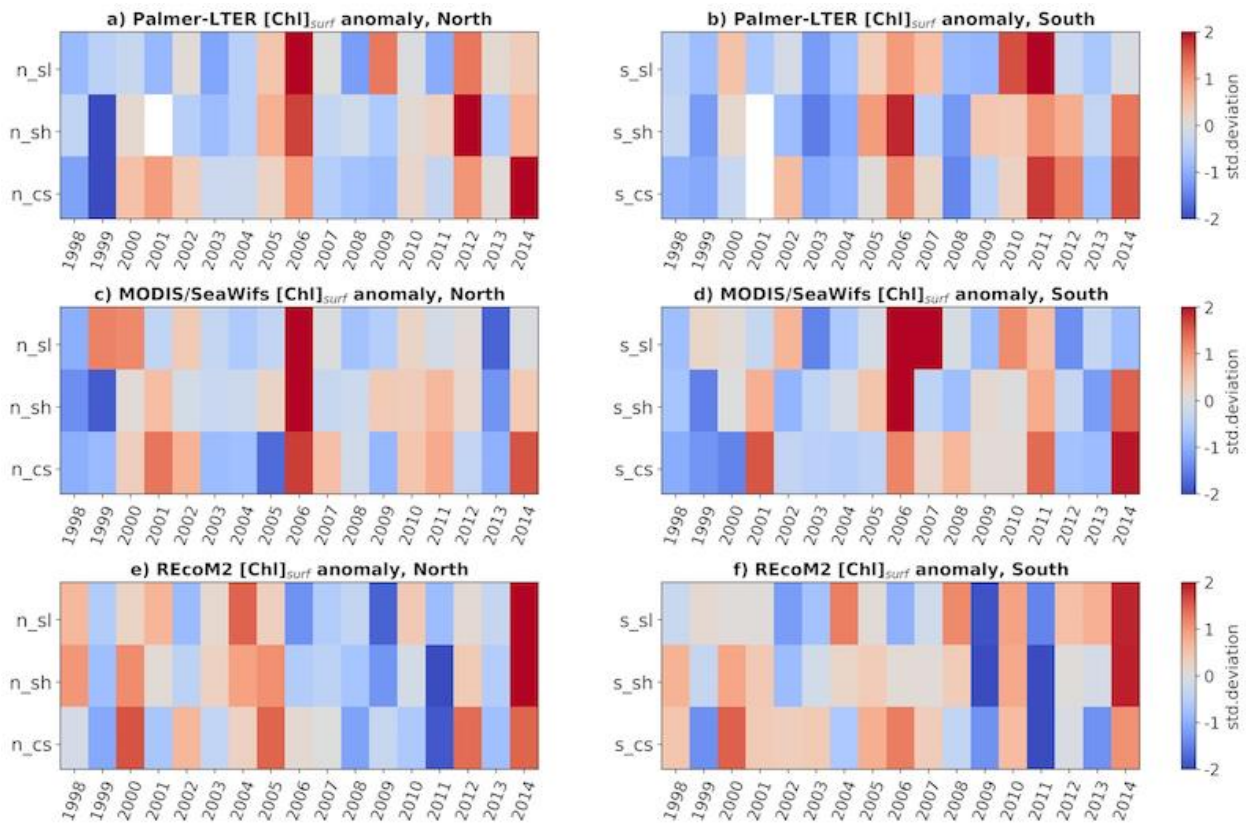
500         Retreat of sea-ice can be early during some sub-regions and late in others (Figure S3),  
501 depending on temperature and wind patterns throughout the season. Sea-ice ridging in the  
502 coastal areas can happen as sea-ice gets pushed from the slope and shelf areas. In the years in  
503 which sea-ice retreat happened consistently early in all sub-regions, such as 1999 and 2009,  
504 surface chlorophyll anomalies were mostly negative or close to neutral in all datasets, while  
505 years of consistent late sea-ice retreat like 2005 and 2014 showed mostly positive or low  
506 negative anomalies. The exception for this pattern is coastal chlorophyll anomalies from the  
507 MODIS/SeaWifs dataset in 2005, which showed negative anomalies. In 2005, however, satellite  
508 images were scarce in the coastal region (1 in the northern coast and 4 in the southern coast),  
509 and it is possible that the satellite data missed the peak of the bloom during this season.

510         It is also worth noting that one of the limitations of the model is that it does not have  
511 interannual variability in the glacial discharge. This could be the cause of the lower chlorophyll  
512 concentrations simulated in some of the years in which satellite and cruise data show large  
513 blooms, such as 2006 and 2011. The year 2011 is one of the only years for which dFe data is  
514 available, and Annett et al. (2017) found that this year had much larger dFe and glacial  
515 meltwater concentrations compared to 2010 and 2012, particularly in the southern region,  
516 leading to an anomalously productive season. This was also a year of anomalously early sea-ice  
517 retreat, which would otherwise lead to an early bloom and deeper MLD in January, usually  
518 indicative of lower chlorophyll concentrations during this month.

519         Although there are marked differences between the MODIS/SeaWifs and Palmer LTER  
520 data, the correlations in time (using the January means for satellite and model data, and cruise  
521 data) calculated for the surface chlorophyll for each sub-region range from 0.52 in the northern  
522 slope to 0.73 in the southern shelf and are larger than the correlations between these datasets  
523 and the model data (Table S1). The only significant correlation for the simulated data was with

524 the Palmer-LTER data in the northern coast (0.57). In years in which all sub-regions showed  
 525 anomalous early or late sea-ice retreat (Figure S3), however, there was agreement between the  
 526 datasets on whether this was a high or low chlorophyll year in January. The seasons of 1998-  
 527 1999 and 2008-2009 were chosen to represent years of early sea-ice retreat, with negative  
 528 chlorophyll anomalies in all datasets; and 2004-2005 and 2013-2014 were chosen to represent  
 529 years of late sea-ice retreat, with positive chlorophyll anomalies. Although 2011 also showed  
 530 early sea-ice retreat, it was not considered in analyses in the next sections due to the  
 531 anomalously high dFe observed, which would mean it does not necessarily represent the  
 532 mechanisms that took place during the other low-ice years.

533  
 534



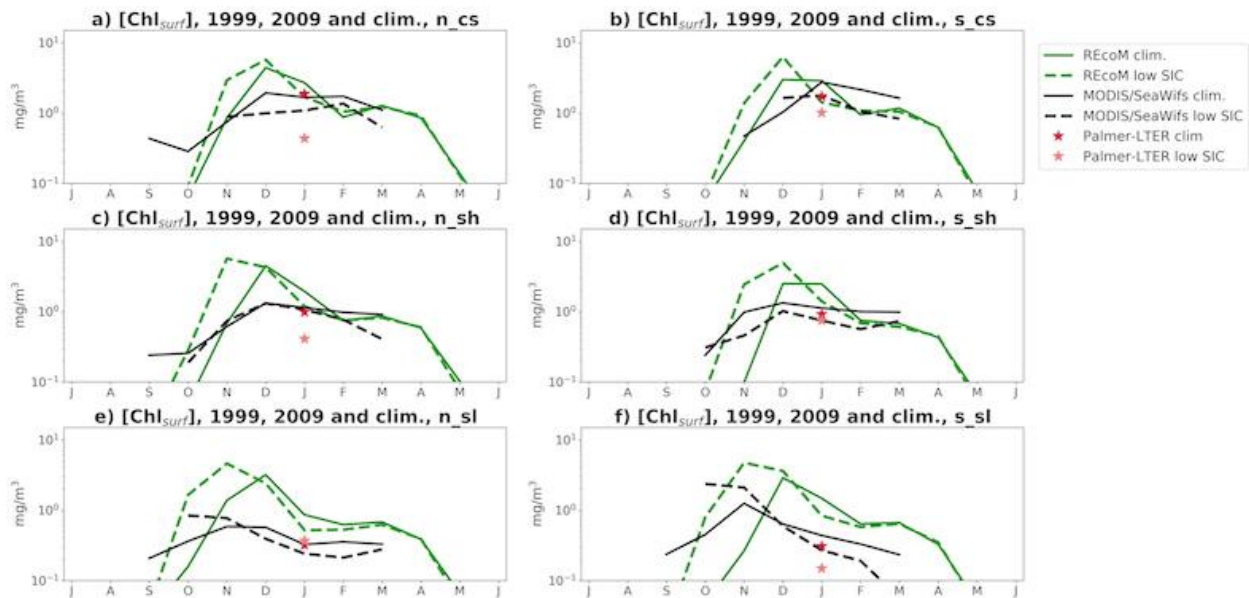
535  
 536 **Figure 5:** Surface chlorophyll concentration anomalies, relative to the cruise climatology for Palmer-LTER  
 537 data (a,b), and relative to January climatology for MODIS/SeaWifs (c, d) and MITgcm-REcoM2 (e, f); for  
 538 northern region (a, c, e) and southern region (b, d, f).

539

540  
541  
542  
543  
544  
545  
546  
547  
548  
549  
550  
551

### 3.8 Phytoplankton blooms in seasons of early and late sea-ice retreat

To compare the differences between years of early sea-ice retreat and the climatology, the monthly geometric mean surface chlorophyll concentration for the early sea-ice retreat seasons (1998-1999, 2008-2009) were calculated for the satellite and model data and plotted against the monthly climatology (Figure 6). The Palmer LTER data is considered as a January mean, and is also plotted in the same figure. The model output suggests an earlier bloom compared to the climatology in the years of early sea-ice retreat. In the satellite data, this trend is observed in the slope region, and hard to determine in the coastal region given the lack of data during the spring and early summer.



552  
553  
554  
555  
556  
557  
558

**Figure 6:** MITgcm-REcoM2 (green) and MODIS/SeaWifs (black) log<sub>10</sub>-transformed climatological monthly surface chlorophyll concentration (full line) and mean concentration for years of early sea ice retreat (dashed line); Palmer-LTER log-transformed climatological surface chlorophyll concentration (red star, plotted as January mean) and mean for years of early sea ice retreat (pink star), during July-June, for regions n\_cs (a), s\_cs (b), n\_sh (c), s\_sh (d), n\_sl (e), s\_sl (f).

559 By January, however, all datasets agree that surface chlorophyll concentrations are  
560 generally lower than the climatological values, with exception being that Palmer LTER shows  
561 slightly higher concentrations in the northern slope and the satellite data has similar values to  
562 the climatology in the northern shelf. In the model, lower chlorophyll values in January can be  
563 attributed to iron limitation, given that an earlier bloom leads to earlier depletion (Figure S2).  
564 Although the model tends to underestimate MLD (Schultz et al., 2020), the time at which light  
565 limitation is lifted, associated with the sea-ice retreat, is well represented. It is possible that the  
566 higher chlorophyll values (compared to observations) seen in the model are partially fueled by  
567 less light limitation at the bottom of the mixed layer. In 2011, however, deeper than usual MLD  
568 due to very early sea-ice retreat was observed in the coastal and shelf areas during the Palmer  
569 LTER cruise (Schultz et al., 2020), associated with high chlorophyll and dFe concentrations  
570 (Annett et al., 2017). This indicates that although light limitation has a large role in controlling  
571 the timing of the bloom, there is enough PAR in mid-summer to fuel large primary production  
572 even in years of anomalously deep mixed layer, and iron limitation could be the reason for the  
573 lower concentrations observed.

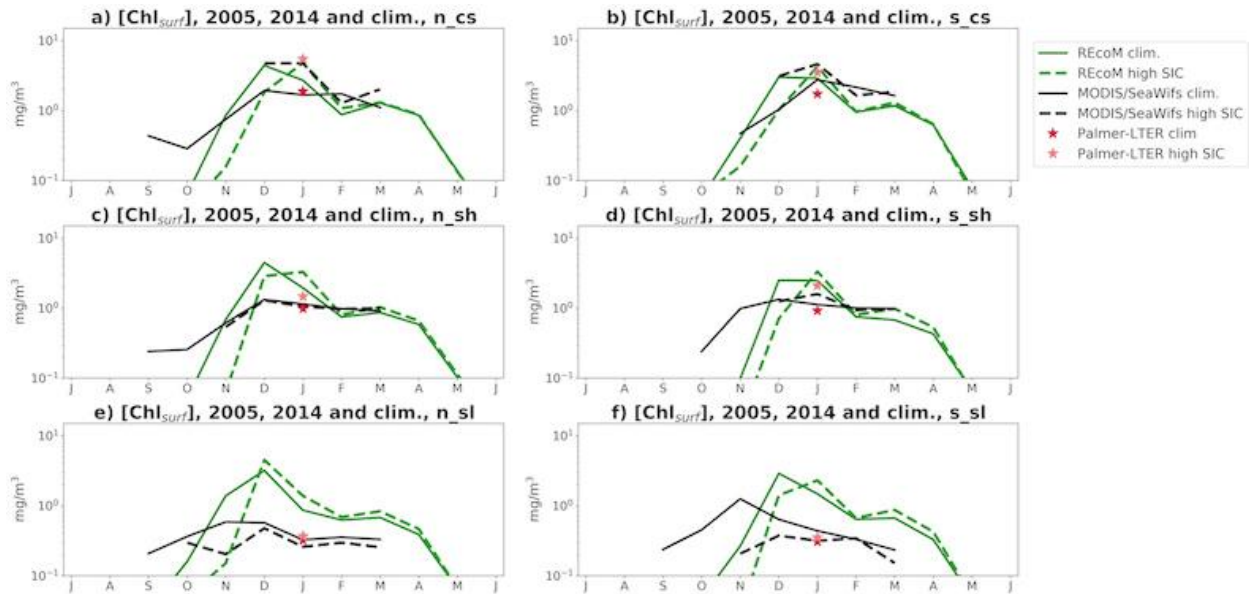
574 During the years of late sea-ice retreat (2004-2005,2013-2014, Figure 7) it is hard to  
575 determine the time of the start of the bloom in the satellite data, given that chlorophyll cannot  
576 be observed earlier in the season due to sea-ice cover. During December and January, however,  
577 the satellite data shows that chlorophyll concentrations are higher than their climatologies in  
578 the coastal region and southern shelf, with values similar to the climatology in the northern  
579 shelf and lower concentrations in the slope region. The Palmer-LTER and model data indicate  
580 higher chlorophyll in all sub-regions by January. In the model, this is due to a late start of the  
581 bloom, leading to a later peak.

582 Overall, despite disagreements in the mean chlorophyll values, all the datasets agree  
583 that the years with early sea-ice retreat had lower chlorophyll concentrations in January while  
584 late sea-ice retreat leads to higher chlorophyll concentrations. While difficult to assess the  
585 progression of the bloom in each set of years from the satellite and cruise data, the model  
586 indicates that less sea ice leads to an earlier bloom and less dFe available by January, with the  
587 opposite happening in years of increased sea ice. While the timing of the bloom is dictated by

588 PAR limitation, the summer concentrations depend on how much dFe has been consumed  
589 earlier in the season.

590

591



592

593 **Figure 7:** MITgcm-REcoM2 (green) and MODIS/SeaWifs (black) log<sub>10</sub>-transformed climatological monthly  
594 surface chlorophyll concentration (full line) and mean concentration for years of late sea-ice retreat  
595 (dashed line); Palmer-LTER log<sub>10</sub>-transformed climatological surface chlorophyll concentration (red star,  
596 plotted as January mean) and mean for years of early sea-ice retreat (pink star), during July-June, for  
597 regions n\_cs (a), s\_cs (b), n\_sh (c), s\_sh (d), n\_sl (e), s\_sl (f). Vertical lines represent standard deviation.

598

599

600

### 3.9 Spatial distribution and interannual variability of DIC

601

602 January monthly mean surface DIC concentrations from the model output were  
603 compared to the Palmer LTER cruise data (Figure 8), with the anomalies relative to the  
604 climatology for each sub-region also shown. The model is able to capture the onshore-offshore  
605 DIC gradient seen in the observations, with lower concentrations towards the coast (Hauri et  
606 al., 2015). However, the simulated values have a bias towards lower concentrations compared  
607 to the cruise data. There are a few limitations in the model that could explain the low bias, one

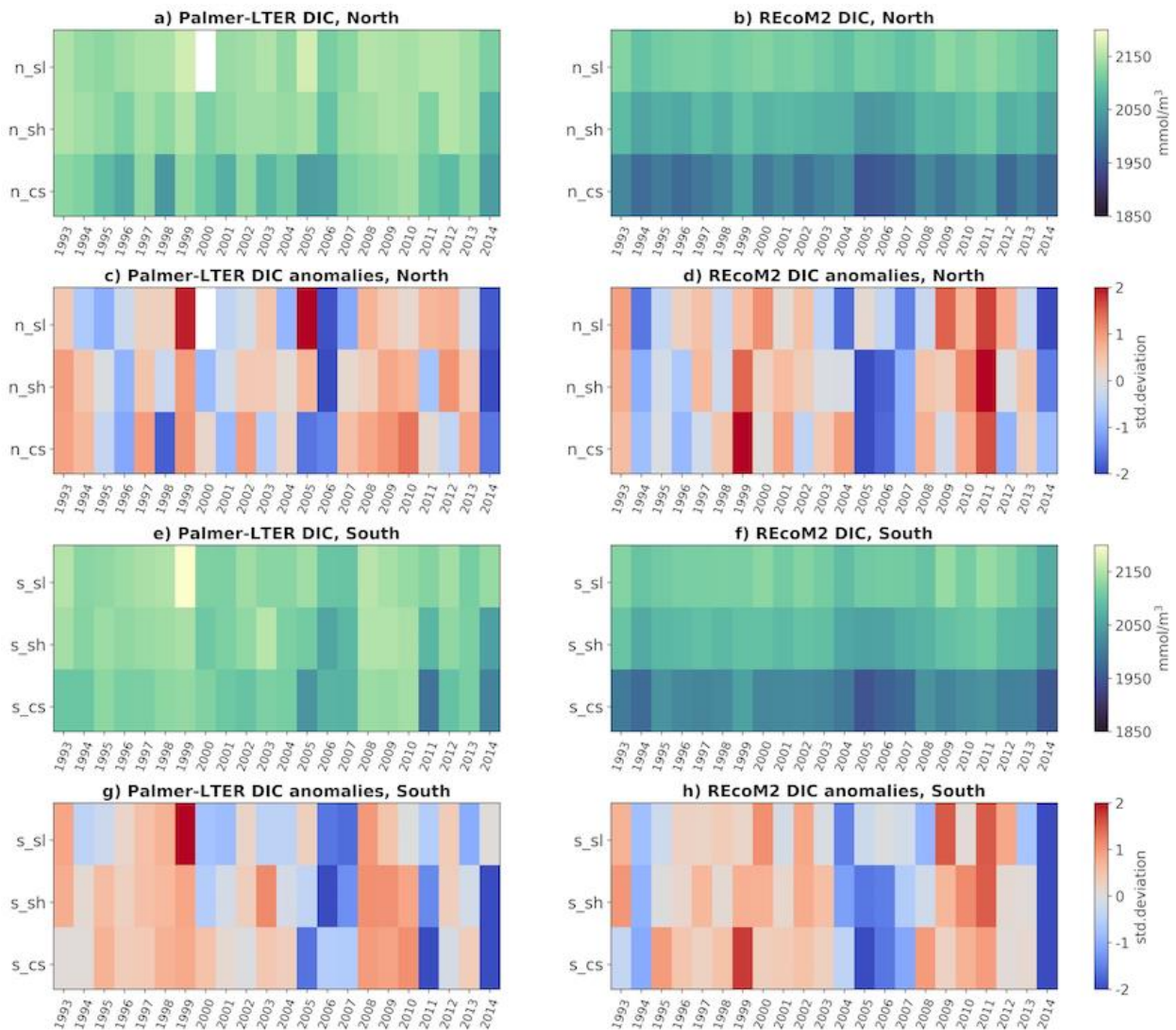
608 of them being that freshwater inputs are added at the surface, which could lead to less mixing  
609 and lower DIC from dilution. Also, the initial and boundary conditions are based on gridded  
610 datasets that are derived from observations mostly collected in open-ocean locations, and  
611 Jones et al. (2017) found that DIC concentrations in Antarctic Circumpolar Water (ACC) derived  
612 water masses were higher in the shelf due to respiration and remineralization as the water  
613 mass makes its way from the slope to the coast. A third reason that could explain the bias  
614 towards lower DIC is that a bias towards higher NPP observed in the model results, which could  
615 also reflect higher net community production and carbon uptake.

616         Despite a bias towards lower concentrations, the interannual variability of simulated DIC  
617 is similar to the variability observed in the Palmer LTER cruise data in most regions, with the  
618 exception of the southern slope (Table S2). DIC variations throughout the season are influenced  
619 by a series of physical and biological mechanisms (Ducklow et al., 2018). The variability of the  
620 physical mechanisms that affect DIC concentrations, which are deepening of the MLD (which  
621 leads to entrainment of high-DIC sub-surface waters) and sea ice melt (which leads to dilution),  
622 are well represented in the model (Schultz et al., 2020). Although the phytoplankton bloom is  
623 patchy and chlorophyll concentration may vary throughout the season at a certain location, the  
624 biological signature of net community production carbon uptake lasts throughout the growth  
625 season (September to the Palmer LTER survey cruise in January). Therefore, the better  
626 agreement between simulated and cruise DIC values compared to the chlorophyll  
627 concentration adds to the evidence that part of the disagreement between the chlorophyll  
628 datasets is due to the patchiness of the data, and that integrated over the season, the biological  
629 processes are better represented in the model.

630         Some of the discrepancies between simulated and cruise DIC are likely to be due to the  
631 same mechanisms as the discrepancies in the chlorophyll values. In 2011, the model is not  
632 capable of capturing the large bloom observed, leading to positive DIC anomalies in the  
633 southern region while the cruise data shows negative anomalies. For the years of early sea-ice  
634 retreat analyzed, both REcoM2 and Palmer-LTER data show positive DIC anomalies, while for  
635 the years of late sea-ice retreat the anomalies are mostly negative with the exception of the  
636 slope region.

637

638



639

640 **Figure 8:** Palmer-LTER (left) and MITgcm-REcoM2 (right) January surface DIC concentrations (a, b, e, f)

641 for north (a, b) and south (e, f) regions; and anomalies relative to the mean (January mean for

642 simulated, and cruise mean for Palmer-LTER, c, d, g, h).

643

644

### 645 3.10 DIC-derived Net Community Production

646

647 Although the DIC anomalies provide an indication of the physical and biological

648 processes that took place throughout the growth season, further quantification is needed to

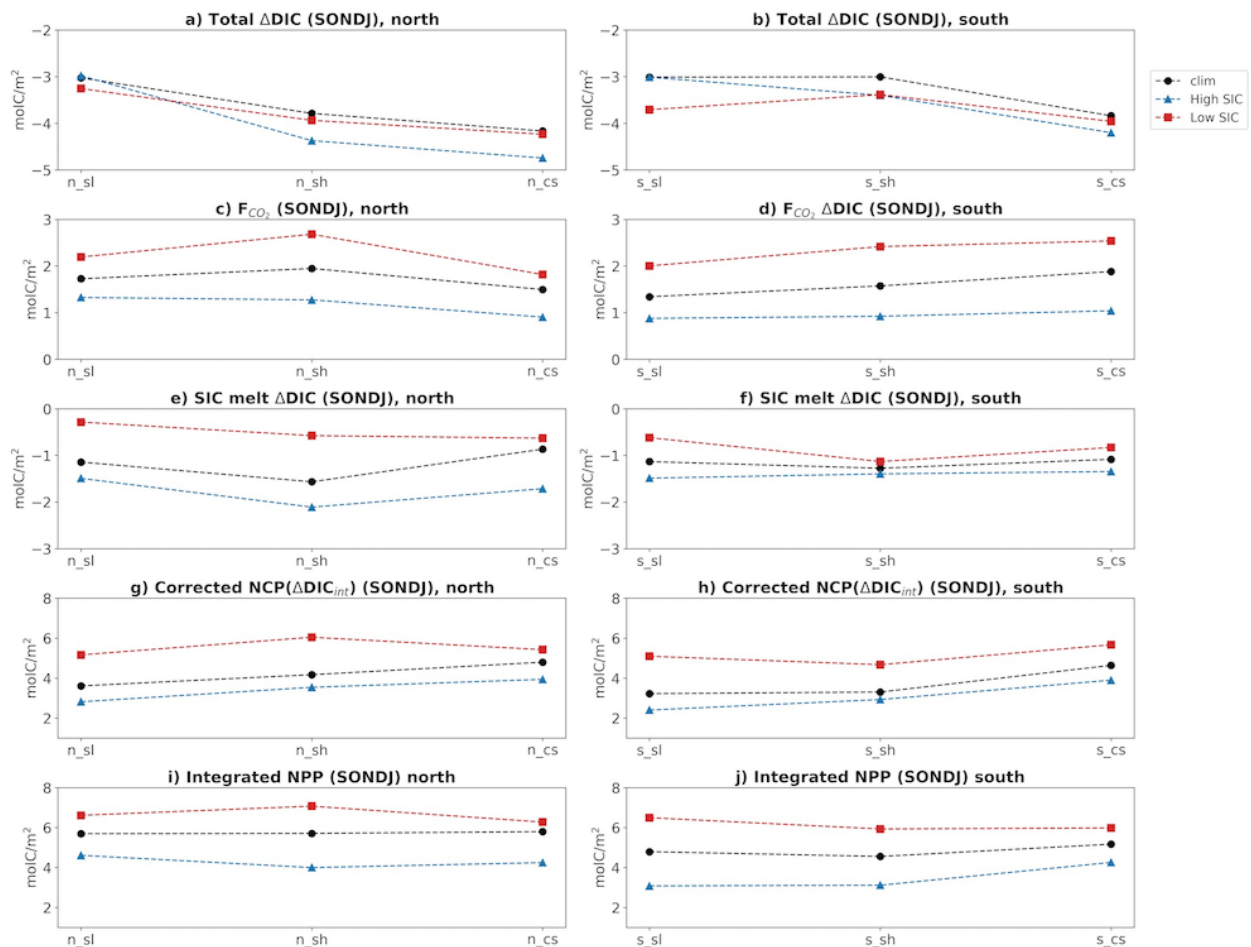
649 assess how much of the DIC drawdown is due to net biological uptake, air-sea fluxes and sea ice  
650 melt. The calculations described in section 2.4 provide an estimate of the influence of each of  
651 these processes in the DIC, and the total DIC drawdown, air-sea CO<sub>2</sub> fluxes, DIC dilution due to  
652 sea ice melt, NCP and seasonally integrated NPP (a diagnostic variable) are shown, for each sub-  
653 region, on Figure 9. January NPP is shown in Figure S5. All these figures include the calculations  
654 for the climatology and for the years of early and late sea-ice retreat described in previous  
655 sections.

656 In a study using Palmer LTER cruise data, Ducklow et al. (2018) find that NCP is  
657 significantly higher than measured export flux, a conclusion that is also reached by other  
658 studies (Buessler et al., 2010; Weston et al., 2013; Stukel et al., 2015). Within each year  
659 sampled, the variability of each rate process measured, including NCP, was moderately high in  
660 both space and time and production likely being higher in sunny days (versus cloudy  
661 conditions). The authors also point out that one of the big uncertainties in trying to assess the  
662 relative magnitude of each estimates is the difficulty in specifying the start of the growing  
663 season after sea-ice retreats.

664 Total DIC drawdown is highest in the northern shelf and coastal areas during years of  
665 late sea-ice retreat, compared to the climatology and to years of early sea-ice retreat (Figure 9  
666 a,b). This happens despite NCP being higher in years of early sea-ice retreat throughout the  
667 whole grid (Figure 9 g,h). The largest drawdown was observed in the northern coast, with a  
668 climatological decrease of 4.16 molC/m<sup>2</sup> during the season that reached 4.74 molC/m<sup>2</sup> during  
669 years of late sea-ice retreat. Higher NCP in years of low SIC is consistent with the satellite  
670 estimates of Li et al. (2015), who found that variations in NCP were linked to sea ice, and that  
671 annually integrated NCP was higher with higher sea surface temperature and longer bloom  
672 season. The larger DIC drawdown despite lower NCP indicates a strong influence of physics in  
673 the inorganic carbon cycle. With increased sea ice throughout the season, there is less air-sea  
674 transfers (which are a source of DIC) and more dilution by late summer.

675 In previous studies using Palmer LTER cruise data, Hauri et al. (2015) found that DIC was  
676 driven by increased biological activity in the south of the WAP and by increased meltwater  
677 towards the north, and Eveleth et al. (2017) found that physical processes had a more

678 pronounced influence in the southern onshore region where active sea-ice melt was still  
 679 happening. The model results show that although climatological summer meltwater values  
 680 (December to February) are higher in the southern part of the grid (Schultz, et al.,2020),  
 681 integrated over spring and summer sea-ice melt has a larger influence in the northern WAP in  
 682 years of late sea-ice retreat, and larger influence in the southern part in years of early sea ice  
 683 retreat (Figure 9 e, f). The calculation performed to account for the influence of meltwater  
 684 takes into account the depth of the MLD, which is shallower in the northern part of the grid  
 685 (Schultz et al., 2020), increasing the effect of melt. Both sea-ice melt and primary production  
 686 tend to be higher in the southern part of the grid by January and February when the Palmer  
 687 LTER cruise takes place, but the relative importance of each process varies from year to year.  
 688  
 689  
 690



692 **Figure 9:** Seasonally integrated (between September and January) total vertically integrated DIC  
693 drawdown (a, b), air-sea CO<sub>2</sub> flux (c, d), effect of sea-ice melt on DIC concentration (e, f), DIC-derived  
694 NCP corrected for air-sea flux and sea ice melt (g, h) and NPP (i, j) for the northern (left) and southern  
695 (right) regions. The sign reflects the effect on the DIC inventory, so that positive F<sub>CO2</sub> reflects a flux into  
696 the ocean and negative meltwater influence reflects dilution. Shown for climatology (black), years of  
697 early sea-ice retreat (red, 1998-1999, 2008-2009) and years of late sea-ice retreat (blue, 2004-2005,  
698 2013-2014).

699

700 Evidence that both biological and physical processes can lead to anomalously high DIC  
701 drawdown is seen in the shelf sub-regions, where both years of early and late sea-ice retreat  
702 show more DIC drawdown than the climatological values. In years of early retreat, the low  
703 dilution by meltwater and increased DIC input by air-sea CO<sub>2</sub> fluxes is compensated by the  
704 higher NCP, which reaches values as high as 6.04 molC/m<sup>2</sup> in the northern shelf. In years of high  
705 SIC, however, low air-sea fluxes and higher meltwater content keep the DIC drawdown below  
706 climatological values despite the low NCP. The WAP is a sink of atmospheric carbon throughout  
707 the season in all years, but the amount of carbon the ocean uptakes depends on the duration of  
708 the ice-free season.

709 Years of high SIC show higher productivity in January, and overall higher DIC drawdown.  
710 If NPP and NCP are integrated over the spring and summer seasons, however, it is seen that this  
711 is because of the timing of the bloom associated with the effect of physics in the DIC  
712 drawdown, not because of higher productivity. While January high chlorophyll values are  
713 accompanied by larger DIC drawdowns, these effects are not directly linked, although they are  
714 both driven by the timing and magnitude of sea-ice melt. Years of low SIC also show more DIC  
715 drawdown than the climatology, driven by the higher NCP throughout the season. Despite the  
716 high NCP, years of early sea-ice retreat still show positive DIC anomalies in January. The  
717 anomalies, however, reflect the positive anomalies that are observed at the beginning of the  
718 season (Figure S5), which are also positive possibly due to increased mixing with DIC-rich  
719 subsurface waters under lower SIC.

720

721 **4 Discussion and Conclusions**

722

723           The MITgcm-REcoM2 model implemented for the west Antarctic Peninsula (WAP) is able  
724 to represent the main patterns observed in the phytoplankton bloom, such as higher  
725 concentrations onshore and progression of the bloom from north to south and offshore to  
726 onshore. The onshore-offshore chlorophyll gradient seen in the observations, however, is not  
727 as pronounced in the model simulation. Li et al. (2015) find that the annually integrated net  
728 community production (NCP) in the coastal areas is up to 8 times higher than what is observed  
729 offshore, and Vernet et al. (2008) finds that primary production ranges from 500-750 mgC/m<sup>2</sup>d  
730 shoreward of the continental slope and from 250-400 mgC/m<sup>2</sup>d over the slope region. In the  
731 model, January net primary production (NPP) is 2.25 times higher in the coastal region  
732 (compared to the slope) in the northern region, and 1.91 times higher in the southern region.  
733 Integrated over September-January, however, the whole grid shows comparable NPP.

734           Comparing chlorophyll values among the different datasets (cruise, satellite and model)  
735 is challenging given that the phytoplankton bloom in the WAP is highly variable and patchy, and  
736 there are gaps in the temporal and spatial coverage of the observations. Some of the  
737 discrepancies observed between datasets in the chlorophyll anomalies, therefore, are likely  
738 attributable to timing of the sampling. Dissolved inorganic carbon (DIC) anomalies in mid-  
739 summer, on the other hand, are the result of the cumulative effect of processes that took place  
740 throughout the season. The model captures well the climatological spatial pattern in the  
741 summer surface DIC field with larger seasonal drawdown and dilution onshore, and the model  
742 is able to reproduce much of the interannual variability seen in the DIC measurements from the  
743 Palmer LTER cruises. We can estimate the importance of biological and physical processes in  
744 driving DIC drawdown each year knowing that the model predicts higher seasonally integrated  
745 productivity in years of low SIC in accordance to the literature and that sea ice and MLD  
746 variability are well represented in the model (Schultz et al., 2020).

747           In years of early sea-ice retreat, both observations (satellite and cruise) and model data  
748 show lower chlorophyll concentrations in January compared to the climatology. While January  
749 NPP is also lower than climatology, seasonally integrated NPP (September to January) is higher,  
750 with a longer productive season due to light limitation being lifted earlier. Surface DIC

751 drawdown during the same period, however, is lower despite the increased NPP. This can be  
752 attributed to the increased air-sea CO<sub>2</sub> fluxes and to decreased dilution by sea ice melt. Years of  
753 late sea-ice retreat, on the other hand, show higher than climatological chlorophyll  
754 concentrations in January in all the datasets analyzed. The model results indicate that these  
755 years exhibit NPP higher than the climatology for January, but overall less seasonally integrated  
756 NPP. The longer sea-ice season also leads to a smaller sink of atmospheric CO<sub>2</sub> and increased  
757 influence of sea-ice melt, resulting in larger DIC drawdown between September and January.

758         Although it is hard to estimate when the bloom starts in the satellite data due to cloud  
759 and sea-ice cover, in the model results the January chlorophyll concentration anomalies are a  
760 result of the timing of the bloom; with late sea-ice retreat, the light limitation is lifted later in  
761 the year and the bloom is closer to its peak in January, while early sea-ice retreat leads to an  
762 earlier bloom and a weaker phytoplankton bloom in January, with the productivity decreasing  
763 due to lower iron concentrations. The model results are consistent with DIC concentrations  
764 deviating from the dilution curve, with lower concentrations than expected, in January during  
765 years of high chlorophyll concentrations as found in Hauri et al. (2015), but our results suggest  
766 that sea-ice melt also plays an important role in driving the seasonal DIC drawdown. Air-sea CO<sub>2</sub>  
767 fluxes have a much larger influence in counteracting the drawdown by biological activity in  
768 years of early sea-ice retreat, due to longer ice-free season.

769         Since ocean dissolved iron (dFe) data is scarce, building initial and boundary conditions  
770 for this micronutrient is a challenge. Given that iron is thought to be the limiting factor  
771 offshore, and that complete iron limitation is not encountered in the model, we suspect that  
772 the initial and boundary conditions overestimate dFe, which is supplied in excess in the offshore  
773 region due to mixing with iron-rich subsurface waters. The lack of iron data is not only a  
774 limitation to build reliable forcings for the model, but also to understand the mechanisms  
775 governing the phytoplankton spatial and temporal variability in the WAP. The role of different  
776 sources of dFe in the WAP biogeochemistry, therefore, is a question that requires future  
777 research and increased field sampling.

778         Interannual variability of glacial sources of freshwater and dFe are also missing.  
779 Although there is substantial melting of glacial waters on the continent, most of it freezes

780 before reaching the ocean (Van Wesseem et al., 2016). The re-freezing of glacial melt impedes  
781 the estimation of yearly runoff to the ocean, although a climatology can be obtained using the  
782 mass balance over a larger time scale. Some of the discrepancies in chlorophyll concentration  
783 between model and data are attributed to the lack of interannual variability in the glacial dFe  
784 input. In 2011, Annett et al. (2017) found anomalously high dFe concentrations linked to  
785 increased glacial meltwater, which in turn led to large and positive chlorophyll anomalies. This  
786 was a warm year with very early sea-ice retreat, and the high chlorophyll concentration differs  
787 from what is observed in other years of early SIC retreat (decreasing bloom by January). It  
788 seems likely, therefore, that 2011 was indeed an anomalous year with high glacial input leading  
789 to a sustained large bloom, and that the lack of interannual variability in the glacial inputs in the  
790 model prevented it from representing the high bloom.

791 Sherrell et al. (2018) found that dFe near Palmer Deep (on the northern, coastal part of  
792 the grid) is provided by sediment sources in coastal, shallower areas, which is then advected to  
793 the shelf region. The authors also argue that the difference from the hypothesis proposed by  
794 Annett et al. (2017), that dFe is mostly from glacial origin, could be due to regional differences  
795 or due to errors in the data interpretation of Annett et al. (2017), which would be caused by  
796 vertical mixing weakening the  $^{18}\text{O}$  isotope signature used to estimate the origin of the  
797 freshwater in that study. The model results suggest that sediment sources of dFe are important  
798 in the coastal regions, and that part of the dFe in the northern shelf is also of sedimentary  
799 origin. In the southern coast, however, glacial inputs and mixing with subsurface waters are  
800 much larger sources of dFe than sediments. Our results, therefore, indicate that there are  
801 regional differences in how iron is provided.

802 Since the model was able to reproduce much of the variability related to sea ice without  
803 meltwater accounting for a source of dFe, we hypothesize that sea ice controls the blooms  
804 through its influence in the physics of the ocean, but that it is not a significant source of dFe.  
805 This conclusion stands even assuming that the magnitude of dFe sources are inaccurate, since  
806 the physics of the model is sufficiently well represented to assume that the distribution of the  
807 iron inputs is accurate.

808           The MITgcm-REcoM2 model results help to fill in the gaps in understanding the link  
809 between the ocean biology, chemistry and physics in the WAP earlier in the warm season, when  
810 the presence of clouds and sea ice hinders the acquisition of satellite and cruise data. Further  
811 quantification of each process in driving carbon sinks in the area rely on acquiring more spring  
812 and early summer data, and will greatly benefit from sampling efforts currently being deployed  
813 using moorings, buoys and gliders. Our results suggest that early sea ice retreat leads to an  
814 earlier bloom, with overall higher productivity during the summer season but lower chlorophyll  
815 concentrations in January. In years of late sea ice retreat, the bloom is closer to the peak in  
816 January, but the associated larger drawdown in DIC also reflects smaller air-sea CO<sub>2</sub> fluxes and  
817 increased sea ice melt. If the trends towards longer ice-free seasons and increased glacial melt  
818 persists, it is likely that the WAP will be a larger sink of atmospheric carbon with increased NCP.

819

820

## 821 **Acknowledgements**

822 The authors thank the scientists, students, technicians and ship crew, officers and captains  
823 involved in collecting Palmer LTER time series data. C. Schultz, S. Doney, M. Kavanaugh and O.  
824 Schofield acknowledge support by the US National Science Foundation (grant PLR-1440435),  
825 and C. Schultz and S. Doney acknowledge support from the University of Virginia. The MITgcm  
826 model is an open source model (mitgcm.org). The version used in this study, with added  
827 parameterizations and specific configurations, are on C. Schultz's github  
828 ([https://github.com/crisoceano/WAP\\_MITgcm](https://github.com/crisoceano/WAP_MITgcm)). Copies of the forcing files needed for the  
829 simulations are in four separate records on zenodo.org, under DOIs 10.5281/zenodo.3627365,  
830 10.5281/zenodo.3627564, 10.5281/zenodo.3627742, and 10.5281/zenodo.4342315.

831

832

## 833 **References**

834

835 Annett, A.L., Skiba, M., Henley, S.F., Venables, H.J., Meredith, M.P., Statham, P.J., Ganeshram,  
836 R.S. (2015) Comparative roles of upwelling and glacial iron sources in Ryder Bay, coastal west  
837 Antarctic Peninsula, *Marine Chemistry*, 176, 21-33. Doi: [10.1016/j.marchem.2015.06.017](https://doi.org/10.1016/j.marchem.2015.06.017)  
838

839 Annett, A.L., Fitzsimmons, J.N., Séguret, M.J.M., Lagerström, M., Meredith, M.P., Schofield, O.  
840 & Sherrell, R.M. (2017) Controls on dissolved and particulate iron distributions in surface waters  
841 of the Western Antarctic Peninsula shelf. *Marine Chemistry*, 196, 81-97.  
842 doi:10.1016/j.marchem.2017.06.004.  
843

844 Arrigo, K.R., van Dijken, G., Long, M. (2008) Coastal Southern Ocean: A strong anthropogenic  
845 CO<sub>2</sub> sink, *Geophysical Research Letters*, 35, L21602. Doi:10.1029/2008GL035624  
846

847 Arrigo, K.R., van Dijken, G.L., Alderkamp, A.C., Erickson, Z.K., Lewis, K.M., Lowry, K.E., Joy-  
848 Warren, H.L., Middag, R., Nash-Arrigo, J.E., Selz, V., van de Poll, W. (2017) Early spring  
849 phytoplankton dynamics in the western Antarctic Peninsula. *Journal of Geophysical Research –*  
850 *Oceans*, 122, 9350-9369. Doi: 10.1002/2017JC013281  
851

852 Brown, M. S., Munro, D. R., Feehan, C. J., Sweeney, C., Ducklow, H. W., Schofield, O. 2019.  
853 Enhanced oceanic CO<sub>2</sub> uptake along the rapidly changing West Antarctic Peninsula. *Nature*  
854 *Climate Change*. DOI: 10.1038/s41558-019-0552-3  
855

856 Buessler, K.O., McDonnell, A.M.P., Schofield, O.M.E., Steinberg, D.K., Ducklow, H.W. (2010) High  
857 particle export over the continental shelf of the west Antarctic Peninsula, *Geophysical Research*  
858 *Letters*, 37, L22606. Doi:10.1029/2010GL045448  
859

860 Carrillo, C.J., Smith, R.C., Karl, D.M. (2004) Processes regulating oxygen and carbon dioxide in  
861 surface waters west of the Antarctic Peninsula, *Marine Chemistry*, 84, 161-179.  
862 Doi:10.1016/j.marchem.2003.07.004  
863

864 Carvalho, F., Kohut, J., Oliver, M. J., Sherrell, R. M., Schofield, O. (2016) Mixing and  
865 phytoplankton dynamics in a submarine canyon in the West Antarctic Peninsula. Journal of  
866 Geophysical Research DOI: [10.1002/2016JC011650](https://doi.org/10.1002/2016JC011650)  
867

868 Comiso, J. C., (2017), Bootstrap Sea Ice Concentrations from Nimbus-7 SMMR and DMSP SSM/I-  
869 SSMIS, Version 3. Boulder, Colorado USA. NASA National Snow and Ice Data Center Distributed  
870 Active Archive Center. doi: [10.5067/7Q8HCCWS4I0R](https://doi.org/10.5067/7Q8HCCWS4I0R)  
871

872 Cook, A.J., Fox, A.J., Vaughan, D.G. & Ferrigno, J.G. (2005), Retreating glacier fronts on the  
873 Antarctic Peninsula over the past half-century. *Science*, 308, 541-544.  
874 doi:[10.1126/science.1104235](https://doi.org/10.1126/science.1104235)  
875

876 Dierssen, H.M. and Smith, R.C. (2000), Bio- optical properties and remote sensing ocean color  
877 algorithms for Antarctic Peninsula waters. Journal of Geophysical Research: Oceans, 105(C11),  
878 26301-26312. Doi: [10.1029/1999JC000296](https://doi.org/10.1029/1999JC000296)  
879

880 Ducklow, H.W., W.R. Fraser, M.P. Meredith, S.E. Stammerjohn, S.C. Doney, D.G. Martinson, S.F.  
881 Sailley, O.M. Schofield, D.K. Steinberg, H.J. Venables, and C.D. Amsler (2013) West Antarctic  
882 Peninsula: An ice-dependent coastal marine ecosystem in transition, *Oceanography*, 26(3), 190-  
883 203. Doi:[10.5670/oceanog.2013.62](https://doi.org/10.5670/oceanog.2013.62)  
884

885 Ducklow, H.W., A. Clarke, R. Dickhut, S.C. Doney, H. Geisz, K. Huang, D.G. Martinson, M.P.  
886 Meredith, H.V. Moeller, M. Montes-Hugo, O. Schofield, S.E. Stammerjohn, D. Steinberg, and W.  
887 Fraser (2012) The marine ecosystem of the West Antarctic Peninsula, in *Antarctica Ecosystems:  
888 An Extreme Environment in a Changing World*, 121-159pp, ed. A.D. Rogers, N.M. Johnston, E.J.  
889 Murphy, and A. Clarke, Wiley-Blackwell, ISBN: 978-1-4051-9840-0.  
890

891 Ducklow, H.W., Stukel, M.R., Eveleth, R., Doney, S.C., Jickells, T., Schofield, O., Baker, A.R.,  
892 Brindle, J., Chance, R., Cassar, N., (2018). Spring-summer net community production, new

893 production, particle export and related water column biogeochemical processes in the marginal  
894 sea ice zone of the West Antarctic Peninsula 2012-2014, *Philosophical Transactions of the Royal*  
895 *Society A*, 20170177. Doi:10.1098/rsta.2017.0177

896

897 Eveleth, R., Cassar, N., Sherrell, R.M., Ducklow, H., Meredith, M.P., Venables, H.J., Lin, Y., and Li,  
898 Z., (2017) Ice melt influence on summertime net community production along the Western  
899 Antarctic Peninsula, *Deep Sea Research Part II: Topical Studies in Oceanography*, 139, 89-102.

900 Doi:10.1016/j.dsr2.1016.07.016

901

902 Eveleth, R., Cassar, N., Doney, S. C., Munro, D. R., Sweeney, C., (2017) Biological and physical  
903 controls on O<sub>2</sub>/Ar, Ar and pCO<sub>2</sub> variability at the Western Antarctic Peninsula and in the Drake  
904 Passage, *Deep Sea Research Part II: Topical Studies in Oceanography*, 139, 77-88.

905 Doi:10.1016/j.dsr2.2016.05.002

906

907 Garcia, H. E., R. A. Locarnini, T. P. Boyer, J. I. Antonov, O.K. Baranova, M.M. Zweng, J.R. Reagan,  
908 D.R. Johnson (2014) *World Ocean Atlas 2013, Volume 4: Dissolved Inorganic Nutrients*

909 (*phosphate, nitrate, silicate*). S. Levitus, Ed., A. Mishonov Technical Ed.; NOAA Atlas NESDIS 76,  
910 25 pp.

911

912 Garibotti, I.A., Vernet, M., Ferrario, M.E., (2005) Annually recurrent planktonic assemblages  
913 during summer in the seasonal ice zone west of the Antarctic Peninsula (Southern Ocean),

914 *Deep-Sea Research I*, 52, 1823-1841. Doi:10.1016/j.dsr.2005.05.003

915

916 Gruber, N. and S.C. Doney, (2019) Modeling of ocean biogeochemistry and ecology, in  
917 *Encyclopedia of Ocean Sciences* (third edition), ed. J.K. Cochran, Elsevier, 5, 291–302,

918 [doi:10.1016/B978-0-12-409548-9.11409-5](https://doi.org/10.1016/B978-0-12-409548-9.11409-5)

919

920 Hauck, J., Völker, C., Wolf-Gladrow, D.A., Laufkötter, C., Vogt, M., Aumont, O., Bopp, L.,

921 Buitenhuis, E.T., Doney, S.C., Dunne, J., Gruber, N., Hashioka, T., John, J., Le Quéré, C., Lima,

922 I.D., Nakano, H., Séréfian & R., Totterdell, I. (2015), On the Southern Ocean CO<sub>2</sub> uptake and the  
923 role of the biological carbon pump in the 21st century. *Global Biogeochemical Cycles*, 29, 1451-  
924 1470. doi:10.1002/2015GB005140  
925

926 Hauck, J., Kohler, P., WolfGladrow, D., Volker, C., (2016) Iron fertilization and century-scale  
927 effects of open ocean dissolution of olivine in a simulated CO<sub>2</sub> removal experiment,  
928 *Environmental Research Letters*, 11, 024007. Doi:10.1088/1748-9326/11/2/024007  
929

930 Hauri, C., S.C. Doney, T. Takahashi, M. Erickson, G. Jiang, and H.W. Ducklow: 2015: Two decades  
931 of inorganic carbon dynamics along the West Antarctic Peninsula, *Biogeosciences*, 12, 6761-  
932 6779, doi:10.5194/bg-12-6761-2015  
933

934 Holland, P.R., Bruneau, N., Enright, C., Losch, M., Kurtz, N.T. & Kwok, R. (2014), Modeled Trends  
935 in Antarctic Sea Ice thickness. *Journal of Climate*, 27, 3784-3801. doi:10.1175/JCLI-D-13-00301.1  
936

937 Jones, E.M., Fenton, M., Meredith, M.P., Clargo, N.M., Ossebaar, S., Ducklow, H.W., Venables,  
938 H.J., and de Baar, H.J.W., (2017) Ocean acidification and calcium carbonate saturation states in  
939 the coastal zone of the West Antarctic Peninsula, *Deep-Sea Research II*, 139, 181-194. Doi:  
940 10.1016/j.dsr2.2017.01.007  
941

942 Kavanaugh, M.T., Abdala, F.N. Ducklow, H., Glover, D., Schofield, O., Stammerjohn, S., and  
943 Doney, S. C. (2015), Canyon effects on phytoplankton biomass and community structure along  
944 the Western Antarctic Peninsula. *Marine Ecology Progress Series*, 524:11-26. Doi:  
945 10.3354/meps11189  
946

947 Kavanaugh, M.T., Church, M.E, Davis, C.O., Karl, D.M., Letelier, R.M. and S.C. Doney (2018),  
948 ALOHA from the Edge: Reconciling three decades of in situ Eulerian observations and  
949 geographic variability in the North Pacific Subtropical Gyre, *Frontiers of Marine Science*. Doi:  
950 10.3389/fmars.2018.00130

951

952 Key, R.M., Olsen, A., van Heuven, S., Lauvset, S.K., Velo, S., Lin, X., Schirnick, C., Kozyr, A.,  
953 Tanhua, T., Hoppema, M., Jutterstrom, S., Steinfeldt, R., Jeansson, E., Ishi, M., Perez, F.F.,  
954 Suzuki, T., Global Ocean Data Analysis Project, Version 2 (GLODAPv2), ORNL/CDIAC-162, NDP-  
955 P093. Carbon Dioxide Information Analysis Center, Oak Ridge National Laboratory, US  
956 Department of Energy, Oak Ridge, Tennessee, 2015.

957

958 Kim, H., Doney, S.C., Iannuzzi, R.A., Meredith, M.P., Martinson, D.G. & Ducklow, H.W. (2016),  
959 Climate forcing for dynamics of dissolved inorganic nutrients at Palmer Station, Antarctica: An  
960 interdecadal (1993–2013) analysis. *Journal of Geophysical Research: Biogeosciences*, 121 (9),  
961 2369--2389. doi:10.1002/2015JG003311

962

963 Kim, H., Ducklow, H.W., Abele, D., Ruiz Barlett, E.M., Buma, A.G.J., Meredith, M.P., Rozema,  
964 P.D., Schofield, O.M., Venables, H.J., and Schloss, I.R., (2018) Inter-decadal variability of  
965 phytoplankton biomass along the coastal West Antarctic Peninsula. *Philosophical Transactions*  
966 *of the Royal Society A: Mathematical, Physical and Engineering Sciences*, 376 (20170179). Doi:  
967 10.1098/rsta.2017.0179.

968

969 Lauvset, S.K., Key, R.M., Olsen, A., van Heuven, S., Velo, A., Lin, X., Schirnick, C., Kozyr, A.,  
970 Tanhua, T., Hoppema, M., Jutterström, S., Steinfeldt, R., Jeansson, E., Ishii, M., Perez, F.F., Suzuki,  
971 T., Watelet, S. (2016) A new global interior ocean mapped climatology: the 1° x 1° GLODAP  
972 version 2. *Earth System Science Data*, 8, 325-340. Doi:10.5194/essd-8-325-2016

973

974 Legge, O.J., Bakker, D.C.E., Meredith, M.P., Venables, H.J., Brown, P.J., Jones, E.M. & Johnson,  
975 M.T. (2017), The seasonal cycle of carbonate system processes in Ryder Bay, West Antarctic  
976 Peninsula. *Deep Sea Research Part II: Topical Studies in Oceanography*, v. 139, 167-180. doi:  
977 10.1016/j.dsr2.2016.11.006

978

979 Lenton, A., Tilbrook, B., Law, R.M., Bakker, D., Doney, S.C., Gruber, N., Ishii, M., Hoppema, M.,  
980 Lovenduski, N.S., Mearns, R.J., McNeil, B.I., Metzl, N., Mikaloff Fletcher, S.E., Monteiro, P.M.S.,  
981 Rödenbeck, C., Sweeney, C., Takahashi, T., (2013) Sea-air CO<sub>2</sub> fluxes in the Southern Ocean for  
982 the period 1990-2009, *Biogeosciences*, 10, 4037-4054, doi:10.5194/bg-10-4037-2013  
983

984 Li, Z., Cassar, N., Huang, K., Ducklow, H.W., Schofield, O., (2016) Interannual variability in net  
985 community production at the Western Antarctic Peninsula region (1997-2014), *Journal of*  
986 *Geophysical Research: Oceans*, 121, 4748-4762. Doi:10.1002/2015JC011378  
987

988 Long, M.C., Lindsay, K., Holland, M.M., (2015) Modeling photosynthesis in sea ice covered  
989 waters, *Journal of Advances in Modeling Earth Systems*, 07. Doi:10.1002/2015MS000436  
990

991 Luo, C., Mahowald, N., Bond, T., Chuang, P.Y., Artaxo, P., Siefert, R., Chen, Y., Schauer, J., (2008)  
992 Combustion iron distribution and deposition, *Global Biogeochemical Cycles*, 22, GB1012. Doi:  
993 10.1029/2007BG002964  
994

995 Meredith, M.P. & King, J.C. (2005), Rapid climate change in the ocean west of the Antarctic  
996 Peninsula during the second half of the 20<sup>th</sup> century. *Geophysical Research Letters*, 32, 1-5. doi:  
997 10.1029/2005GL024042  
998

999 Montes-Hugo, M., Doney, S.C., Ducklow, H.W., Fraser, W., Martinson, D., Stammerjohn, S.E.,  
1000 Schofield, O., (2009). *Science*, 323, 5920, 1470-1473. Doi:10.1126/science.1164533  
1001

1002 Regan, H.C., Holland, P.R., Meredith, M.P. & Pike, J. (2018), Sources, variability and fate of  
1003 freshwater in the Bellingshausen Sea, Antarctica. *Deep-Sea Research Part I: Oceanographic*  
1004 *Research Papers*, 133, 59-71. doi: 10.1016/j.dsr.2018.01.005  
1005

1006 Schofield, O., Saba, G., Coleman, K., Carvalho A-F., Couto, N., Finkel, Z., Irwin, A., Kahl, A.,  
1007 Montes-Hugo, M., Waite, N. (2017) Decadal variability phytoplankton community composition

1008 in the coastal waters of a warming West Antarctic Peninsula. *Deep Sea Research*.  
1009 doi/10.1016/j.dsr.2017.04.014  
1010

1011 Schultz, C., Doney, S., Zhang, W.G., Regan, H., Holland, P., Meredith, M., and Stammerjohn, S.,  
1012 (2020) Modeling of the influence of sea ice cycle and Langmuir circulation on ocean surface  
1013 mixed layer depth and freshwater distribution off the West Antarctic Peninsula. *Journal of*  
1014 *Geophysical Research: Oceans*. Doi:10.1029/2020JC016109  
1015

1016 Sherrell, R.M., Annett, A.L., Fitzsimmons, J.N., Rocanova, V.J., Meredith, M.P., (2018) A  
1017 'shallow bathtub ring' of local sedimentary iron input maintains the Palmer Deep biological  
1018 hotspot on the West Antarctic Peninsula shelf. *Philosophical Transactions of the Royal Society*,  
1019 A376: 20170171. Doi:10.1098/rsta.2017.0171  
1020

1021 Stammerjohn, S.E., Martinson, D.G., Smith, R.C. & Ianuzzi, R.A. (2008), Sea ice in the western  
1022 Antarctic Peninsula region: Spatio-temporal variability from ecological and climate change  
1023 perspectives. *Deep-Sea Research Part II*, 55, 2041-2058. doi: 10.1016/j.dsr2.2008.04.026  
1024

1025 Stammerjohn, S., Massom, R. A., Rind, D., & Martinson, D. (2012), Regions of rapid sea ice  
1026 change: An inter-hemispheric seasonal comparison. *Geophysical Research Letters*, 39 (L06501).  
1027 doi: 10.1029/2012GL050874  
1028

1029 Stukel, M.R., Asher, E., Couto, N., Schofield, O., Strebels, S., Tortell, P., Ducklow, H.D., The  
1030 imbalance of new and export production in the western Antarctic Peninsula, a potentially  
1031 "leaky" ecosystem, *Global Biogeochemical Cycles*, 29, 1400-1420, 2015.  
1032

1033 Takahashi, T., Sutherland, S.C., Chipman, D.W., Goddard, J.G., Ho, C., Newberger, T., Sweeney,  
1034 C., Munro, D.R., (2014) Climatological distributions of pH, pCO<sub>2</sub>, total CO<sub>2</sub>, alkalinity, and  
1035 CaCO<sub>3</sub> saturation in the global surface ocean, and temporal changes at selected locations,  
1036 *Marine Chemistry*, 164, 95-125. Doi:10.1016/j.marchem.2014.06.004

1037  
1038  
1039  
1040  
1041  
1042  
1043  
1044  
1045  
1046  
1047  
1048  
1049  
1050  
1051  
1052  
1053  
1054  
1055  
1056  
1057  
1058  
1059  
1060  
1061

Van Wesseem, J.M., Meredith, M.P., Reijmer, C.H., van den Broeke, M.R. & Cook, A.J. (2016),  
Characteristics of the modelled meteoric freshwater budget of the western Antarctic Peninsula,  
*Deep Sea Research Part II: Topical Studies in Oceanography*, 139, 31-39.

[doi:10.1016/j.dsr2.2016.11.001](https://doi.org/10.1016/j.dsr2.2016.11.001)

Vernet, M., Martinson, D., Ianuzzi, R., Stammerjohn, S., Kozlowski, W., Sines, K., Smith, R. &  
Garibotti, I. (2008), Primary production within the sea ice zone west of the Antarctic Peninsula: I  
– Sea ice, summer mixed layer, and irradiance. *Deep-Sea Research Part II*, 55, 2068-2085. doi:

[10.1016/j.dsr2.2008.05.021](https://doi.org/10.1016/j.dsr2.2008.05.021)

Wanninkhok, R., (1992) Relationship between wind-speed and gas exchange over the ocean,  
*Journal of Geophysical Research – Ocean*, 97, 7373-7382. Doi:10.1029/92JC00188

Weston K, Jickells TD, Carson DS, Clarke A, Meredith MP, Brandon MA, Wallace MI, Ussher SJ,  
Hendry KR. (2013) Primary production export flux in Marguerite Bay (Antarctic Peninsula):  
Linking upper water-column production to sediment trap flux. *Deep Sea Res. I* 75, 52–66.

[doi:10.1016/j.dsr.2013.02.001](https://doi.org/10.1016/j.dsr.2013.02.001)